

The Metal-Insulator Transition in Mn-Substituted $\text{Sr}_3\text{Ru}_2\text{O}_7$

by a photoemission study

by

Zhi Huai Zhu

B.Sc., Nanjing University, 2007

A THESIS SUBMITTED IN PARTIAL FULFILLMENT OF
THE REQUIREMENTS FOR THE DEGREE OF

MASTER OF SCIENCE

in

The Faculty of Graduate Studies

(Physics)

THE UNIVERSITY OF BRITISH COLUMBIA

(Vancouver)

October, 2009

© Zhi Huai Zhu 2009

Abstract

We have studied the metal-insulator transition (MIT) in Mn-substituted $\text{Sr}_3\text{Ru}_2\text{O}_7$ by x-ray photoemission (XPS) and angle-resolved photoemission spectroscopy (ARPES). In XPS, both the surface- and bulk-sensitive spectra show a two-peak structure, corresponding to the well screened and the unscreened excitations. The evolution of the well screened peak with Mn is that the higher the concentration of Mn impurities, the lower the intensity of the peak, indicating that the screening channels are determined by the metallic property of a system. In ARPES, a strong doping dependence is also observed for the Fermi surface, which loses the 2D sheet associated with the d_{xy} band and reduces to the 1D $d_{xz/yz}$ Fermi surfaces, as the system changes from metal to a Mott insulator. As for the band dispersion, we see that the d_{xy} band shifts in energy toward the chemical potential, becoming degenerate with the $d_{xz/yz}$ bands, to the point of being indistinguishable. A nesting vector $q_{\alpha\beta}=(0.33, 0.33, 0)$ has been determined from the Fermi surface of the 10% Mn doped sample, as in response to-or alternatively inducing-a charge/orbital ordering across the Mott transition. The opening of an energy gap is observed below the MIT both as a function of temperature and Mn substitution. To obtain a microscopic understanding of the MIT, we have performed a local-density approximation calculations for the electronic structures of $\text{Sr}_3\text{Ru}_2\text{O}_7$ and found that spin-orbital coupling induces an unexpected magnetic anisotropy. This might play a key role in the emergence of the MIT and magnetic superstructure in Mn-substituted $\text{Sr}_3\text{Ru}_2\text{O}_7$, as well as the nematic behavior in the parent compound.

Table of Contents

Abstract	ii
Table of Contents	iii
List of Tables	v
List of Figures	vi
Acknowledgements	viii
1 Introduction	1
2 Photoemission Spectroscopy	4
2.1 General Principles	4
2.2 Core-Level X-ray Photoemission Spectroscopy	8
2.2.1 Main lines and satellites	8
2.2.2 Screening by the charge transfer	10
2.2.3 The Zaanen-Sawatzky-Allen model	13
2.2.4 Cluster model	15
2.3 Angle-Resolved Photoemission Spectroscopy	17
3 Suppressed Screening Channel in $\text{Sr}_3(\text{Ru}_{1-x}\text{Mn}_x)\text{O}_7$ by Substitutional Mn doping	20
3.1 Introduction	20
3.2 Experiment	21
3.3 Results and Discussion	23
3.3.1 APE spectra	24

Table of Contents

3.3.2	VOLPE spectra	28
3.3.3	Fitting of the spectra	30
3.3.4	Theoretical interpretation	33
3.4	Conclusion	36
4	ARPES Investigation on MIT in Mn-doped $\text{Sr}_3\text{Ru}_2\text{O}_7$. .	37
4.1	Introduction	37
4.2	Experiment	40
4.3	Results and Discussion	40
4.3.1	Fermi surface	40
4.3.2	Enhanced FS nesting with Mn doping	45
4.3.3	Energy and momentum distribution curves	51
4.3.4	Energy gap opening	57
4.3.5	Band structure calculation	61
4.3.6	General discussion	65
4.4	Conclusion	66
5	Summary	68
	Bibliography	70

List of Tables

3.1	Compound ratio of well screened/main peak intensity	30
4.1	FS volume of α and β sheets with/without Mn doping. . . .	50

List of Figures

1.1	Crystal structure of the layered ruthenates	2
2.1	Schematic picture for the DOS revealed by PES	5
2.2	Electron mean free path as a function of their kinetic energy for various metals.	7
2.3	Schematic picture for XPS and PES spectra	8
2.4	Schematic picture for the charge-transfer process	12
2.5	Schematic electron removal and addition states for a Mott- Hubbard insulator and a charge transfer insulator.	13
2.6	Cluster model for CuO_4 plaquette	16
3.1	Transport measurements of $\text{Sr}_3(\text{Ru}_{1-x}\text{Mn}_x)_2\text{O}_7$	22
3.2	X-ray absorption spectra of $\text{Sr}_3(\text{Ru}_{1-x}\text{Mn}_x)_2\text{O}_7$	22
3.3	Ru $3d$ photoemission spectra of $\text{Sr}_3\text{Ru}_2\text{O}_7$	24
3.4	Mn doping dependence of Ru $3d$ photoemission spectra in $\text{Sr}_3\text{Ru}_{(1-x)\text{Mn}_x}_2\text{O}_7$	25
3.5	Ru $3d$ photoemission spectra in $\text{Sr}_{0.06}\text{Ca}_{1.94}\text{RuO}_4$	26
3.6	Ru $3d$ HAXPES spectra in $\text{Sr}_3\text{Ru}_{(1-x)\text{Mn}_x}_2\text{O}_7$ with $x = 0$ and 0.2	28
3.7	Sr $3d$ HAXPES spectra in $\text{Sr}_3\text{Ru}_{(0.95)\text{Mn}_{0.05}}_2\text{O}_7$	29
3.8	Analysis of relative intensity and energy position of Ru $3d$ peaks in APE	32
3.9	Analysis of relative intensity and energy position of Ru $3d$ peaks in HAXPES	32
3.10	Best fit for APE Ru $3d$ spectra	33

List of Figures

3.11 Core-level spectra from DMFT calculation with two different W/U by Kim <i>et al.</i>	35
3.12 Theoretical Ru $3d$ spectra calculated by Okada and Veenendaal	35
4.1 Simulation of Mn induced spin ordering pattern based on REXS data by Hossain <i>et al.</i>	39
4.2 Raw FS for $\text{Sr}_3(\text{Ru}_{1-x}\text{Mn}_x)_2\text{O}_7$ with $x=0, 0.05$ and 0.1 from ARPES measurements	42
4.3 FS of $\text{Sr}_3\text{Ru}_2\text{O}_7$ in comparison with LDA calculations	43
4.4 Photon energy scan and FS of $\text{Sr}_3\text{Ru}_2\text{O}_7$ measured at $h\nu=120$ eV.	44
4.5 Nesting vector check in FS of $\text{Sr}_3\text{Ru}_2\text{O}_7$	47
4.6 FS of $\text{Sr}_3(\text{Ru}_{0.95}\text{Mn}_{0.05})_2\text{O}_7$	48
4.7 FS of $\text{Sr}_3(\text{Ru}_{0.9}\text{Mn}_{0.1})_2\text{O}_7$	49
4.8 MDC's and intensity plot along Γ -M- Γ in $\text{Sr}_3\text{Ru}_2\text{O}_7$	54
4.9 EDC's and intensity plot along Γ -M- Γ in $\text{Sr}_3\text{Ru}_2\text{O}_7$	54
4.10 MDC's and intensity plot along Γ -M- Γ in $\text{Sr}_3(\text{Ru}_{0.95}\text{Mn}_{0.05})_2\text{O}_7$	55
4.11 EDC's and intensity plot along Γ -M- Γ in $\text{Sr}_3(\text{Ru}_{0.95}\text{Mn}_{0.05})_2\text{O}_7$	55
4.12 MDC's and intensity plot along Γ -M- Γ in $\text{Sr}_3(\text{Ru}_{0.9}\text{Mn}_{0.1})_2\text{O}_7$	56
4.13 EDC's and intensity plot along Γ -M- Γ in $\text{Sr}_3(\text{Ru}_{0.9}\text{Mn}_{0.1})_2\text{O}_7$	56
4.14 Quasiparticle peaks is suppressed and an energy gap is opened during the metal to insulator transition.	59
4.15 Temperature effect on the Fermi edge in 10% Mn doped sample.	59
4.16 Temperature effect on the FS in the undoped and 10% Mn doped sample.	60
4.17 LDA and LDA+SOC band dispersion of $\text{Sr}_3\text{Ru}_2\text{O}_7$	63
4.18 LDA and LDA+SOC band dispersion in the bulk and surface of Sr_2RuO_4	64

Acknowledgements

Many people contributed my fruitful MSc experience at the University of British Columbia and I would like to thank all of them. First of all, I want to express my gratitude to my supervisor Andrea Damascelli, who took care of my scientific training in the last two years, and I also express my deep thanks to Ilya Elfimov, who taught me all the things about LDA calculations.

The support from the quantum material group is extremely important for me to complete my thesis. I want to thank Giorgio Levy and David Fournier firstly, you two taught me everything about running ARPES experiments. Especially, Giorgio, you helped me to run experiments during all my beamtimes, and patiently taught me lots of physics; also I can never forget how good you are being a family man. David, I am really benefited from the Igor code you gave me, which allowed me to easily analyze the data.

I would like to thank Giancarlo Panaccione from Elettra Trieste, who performed the XPS experiments reported in my thesis, and wrote me a recommendation letter which helped me to get a four-years scholarship. Although most of our communications are through e-mail and at phone, I hope to see you sometime again and have more collaborations with you.

I would like to thank Suman Hossain, who did many beautiful XAS and REXS work on the material that I am studying in this thesis. He also helped me a lot at the beginning of my research project. I sincerely wish you have a great life at Stanford University.

I also would like to thank all the other members at my lab, Markus Raichle, Christian Veenstra, Ryan Wicks, and Jonathan Rosen. I have really enjoyed the time spent with you and I am looking forward to a longer happy

Acknowledgements

time with you during my Ph.D study.

Finally, I really want to mention my girlfriend Vicky Li, she gave me tons of support for my heavy workloads in physics, have taken very good care of my daily life, and spent many, many hours waiting for me in the hospital for my unexpected illness. Thank you for all your support, Vicky.

Chapter 1

Introduction

The frontier of modern solid state physics lies in understanding the properties of strongly correlated systems. Because the many-body interactions in these systems, including electron-electron correlations and electron-phonon coupling, give rise to a variety of fascinating phenomena such as: metal-insulator transition (MIT), charge-spin-orbital ordering, quantum magnetism, colossal magneto-resistance, and unconventional superconductivity [a review on correlated electron systems, 2000]. These novel quantum phenomena have triggered extensively studies not only for the possible alternative pathways for the design of new materials and functional devices, which hold so much promise for technological advances in fields as diverse as electronics, spintronics, telecommunications, and computer science, but also for the progress of fundamental science in the form of modern theory of solids. In order to understand fundamental physical properties of these complex systems, the direct observation of electron states is most desirable. Therefore, the photoemission technique, which can measure the electric density of states and the momentum distribution of electrons, provides an unique opportunity to directly uncover how the electrons behave in solids, and it has been extensively performed in different strongly correlated systems so far. As a matter of fact, many of these physical phenomena can often be observed within one single material family by tuning fundamental control parameters like temperature, pressure, and chemical doping. This is the case for many of the transition-metal oxides such as, for instance, the ruthenium oxides which have recently become of the most important material families as far as the study of strongly correlated electrons is concerned. These materials, and in particular the perovskite ruthenium oxides of the Ruddlesden-Popper type $(\text{Sr}/\text{Ca})_{n+1}\text{Ru}_n\text{O}_{3n+1}$ is a good family to study superconductor, fermi liquid,

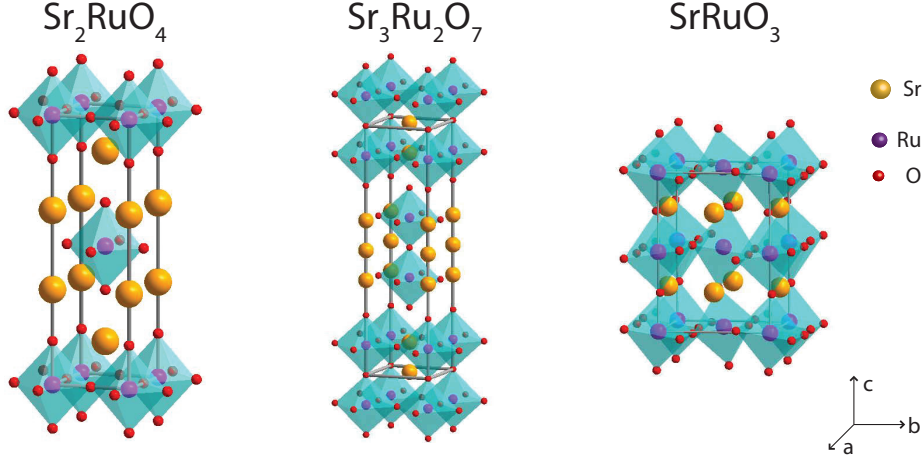


Figure 1.1: The perovskite crystal structures for $\text{Sr}_{n+1}\text{Ru}_n\text{O}_{3n+1}$: Sr_2RuO_4 with $n = 1$, $\text{Sr}_3\text{Ru}_2\text{O}_7$ with $n = 2$ and SrRuO_3 with $n = \infty$.

metamagnetic, magnetic order and MIT. The crystal structures is shown in Fig.1.1. SrRuO_3 ($n = \infty$) and $\text{Sr}_4\text{Ru}_3\text{O}_{10}$ ($n = 3$) are itinerant ferromagnets [Callaghan et al., 1966; Crawford et al., 2002]. The single-layered Sr_2RuO_4 ($n = 1$) is a strongly correlated Fermi liquid and a spin-triplet superconductor [Mackenzie and Maeno, 2003]. The double-layered $\text{Sr}_3\text{Ru}_2\text{O}_7$ ($n = 2$) is essentially paramagnetic with a metamagnetic transition at low temperatures in large magnetic fields [Grigera et al., 2001].

Due to the weak influence of electron correlation effects in the delocalized Ru 4d orbitals, $\text{Sr}_3\text{Ru}_2\text{O}_7$ is also an important material that are extremely sensitive to impurities. With the inclusion of a few percent of Mn, a MIT was observed in transport experiments and the emergence of a Mott-like antiferromagnetic state was proposed [Mathieu et al., 2005]. In this thesis, we focus on the study of the MIT in $\text{Sr}_3(\text{Ru}_{1-x}\text{Mn}_x)_2\text{O}_7$ by using the photoemission technique. Because the MIT is driven by correlations effects associated with the electron-electron interactions [Imada et al., 1998], the study of MIT would be very important for us to understand the electronic, spin correlated behaviors in $\text{Sr}_3\text{Ru}_2\text{O}_7$.

Chapter 1. Introduction

The present thesis is organized as follows. The principle of core level x-ray photoemission (XPS) and angle-resolved photoemission spectroscopy (ARPES) is described in Chapter 2. The experimental results obtained from XPS is shown in the Chapter 3 and the ARPES data is presented in the Chapter 4. Chapter 3 and Chapter 4 have their own introduction, discussions and conclusions related to a specific topic. Chapter 5 gives a summary for the whole thesis.

Chapter 2

Photoemission Spectroscopy

2.1 General Principles

Photoemission spectroscopy (PES) is an extensively used technique in physics, chemistry and biology to investigate the electronic structure of matter. The phenomenon of photoemission was first observed by Hertz [Hertz, 1887] in 1887 and was later explained by Einstein's well known theory of photoelectric effect. This procedure can be briefly described as when a beam of light with energy $h\nu$ hits a solid, an electron in the solid at binding energy E_B will absorb the photons and be emitted as a photoelectron. With the energy conservation, the kinetic energy E_{kin}^{vac} of the photoelectron measured in vacuum is:

$$E_{kin}^{vac} = h\nu - \phi - |E_B|. \quad (2.1)$$

Where we usually define $E_B = 0$ at Fermi energy E_F and ϕ is the work function of the sample [Lang and Kohn, 1971]. In real experiments, E_F is determined by measuring an Au sample, and the E_B of all other samples are calibrated according to the E_F of gold. In order to measure the kinetic energy of photoelectrons, these electrons have to pass through the kinetic energy analyzer into the detector where they are counted. Since the Fermi level of sample and analyzer are equilibrated by electrically connection, and the analyzer also has a work function ϕ_a , the measured kinetic energy E_{kin} is different from the E_{kin}^{vac} and it can be expressed as:

$$E_{kin} = h\nu - |E_B| - \phi_a. \quad (2.2)$$

One of the most attractive features of PES is that the direct information on orbital occupation, namely the electron energy distribution in a material,

2.1. General Principles

is determined, as shown in Fig.2.1. Assuming the electrons in PES are excited from the initial state i with a wavefunction ψ_i to final states f with wavefunction ψ_f , we can calculate the photoemission spectrum by *Fermi's Golden Rule*,

$$I \propto \sum_f |\langle \psi_f | r | \psi_i \rangle|^2 \delta(E_F - E_i - h\nu), \quad (2.3)$$

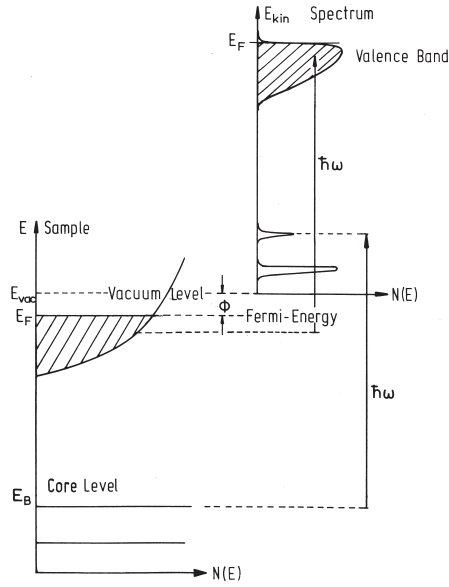


Figure 2.1: Relation between the energy levels in a solid and the electron energy distribution produced by photon energy $\hbar\omega$ [Hüfner, 1995].

In one-electron approximation, the electrons are treated as independent from each other and that removal of one electron from the system will not affect the status of the remaining $(N-1)$ electrons. Under this assumption, the wave functions of both the initial and final states can be expressed by single Slater determinants, and the photoemission spectrum $I(E_B)$ of orbital

2.1. General Principles

k becomes:

$$\begin{aligned} I(E_B) &\propto \sum_k \delta(E_F - E_i - h\nu) \\ &\propto \sum_k \delta(E_B + \varepsilon_k) \\ &\propto N(-E_B) \end{aligned} \tag{2.4}$$

where ε_k is the Hartree-Fock orbital energy of the orbital k , and the relation $E_B = -\varepsilon_k$ based on *Koopmans's theorem* [Koopmans, 1933] is applied. $N(-E_B)$ is the density of state (DOS) at orbital k , which describes the orbital occupation.

However, the one-electron approximation only gives us a glimpse on photoemission spectrum and it does not work for correlated systems. To understand correlated systems, we have to consider a variety of many-body interactions, such as electron-electron coulomb repulsion, and electron-phonon interaction, to obtain the appropriate wave functions of both the initial and final states. On the other hand, the process of the removal of electrons in PES can be described by the three-step model based on sudden approximation. In the first step, an electron is excited to above the Fermi energy by absorbing a photon. In the second step this electron travels inside the sample and eventually goes to the surface. Finally, this electron perhaps get a chance to escape through the sample surface into the vacuum where it will be detected by an energy analyzer. Considering the electron-traveling in the second step, another important concept we want to mention here is the electron escape depth. Usually, electrons emitted by absorbing photons can only travel a few \AA and then become secondary electrons when escaping out of the sample [Hüfner, 1995], a result of collisions with nucleus. This means only the electrons in a very thin layer near the surface of samples will contribute to the intensities of photoemission spectrum. Because of the very short escape depth, atomically clean surfaces are required and a Ultra-Hight Vacuum (UHV) experimental environment is needed to investigate the samples, which have to be prepared *in situ*.

2.1. General Principles

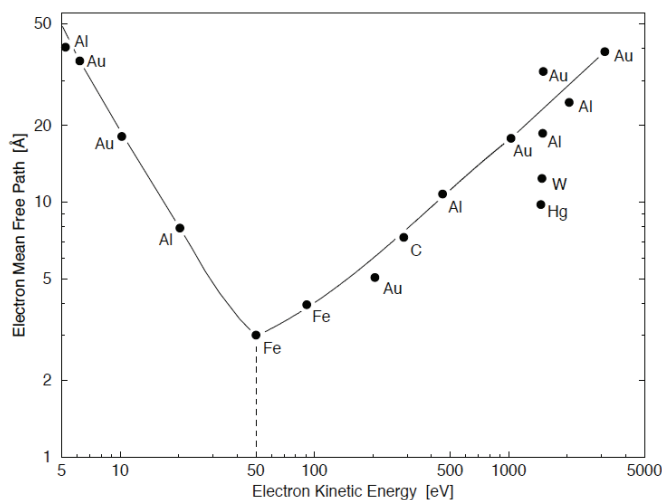


Figure 2.2: Electron mean free path as a function of their kinetic energy for various metals [Hüfner, 1995].

The electron escape length is a very important parameter in PES experiment. Beside its dependence on samples, the E_{kin} of electrons also strongly affects the electron escape length and its relationship with electron mean free path is shown in Fig:2.2. From eq.(2.2), an appropriate incoming photon energy therefore allows us to investigate the core-level or valence excitations by changing E_B , and surface or bulk electrons structures by changing E_K , under an acceptable energy resolution. The energy level of the monochromatic X-ray is generally divided into three regimes. The ultraviolet regime (5-100 eV, UPS) is used to explore the low-energy excitations of the valences bands, the soft X-ray regime (100 – 10³eV, Soft XPS) is used to investigate the core-level excitations of electrons in the sample surface and the hard X-ray regime (10³ – 10⁴eV, Hard XPS) has to be achieved by synchrotron radiation and is used to study the core-level excitation of electrons in the bulks of the sample.

2.2. Core-Level X-ray Photoemission Spectroscopy

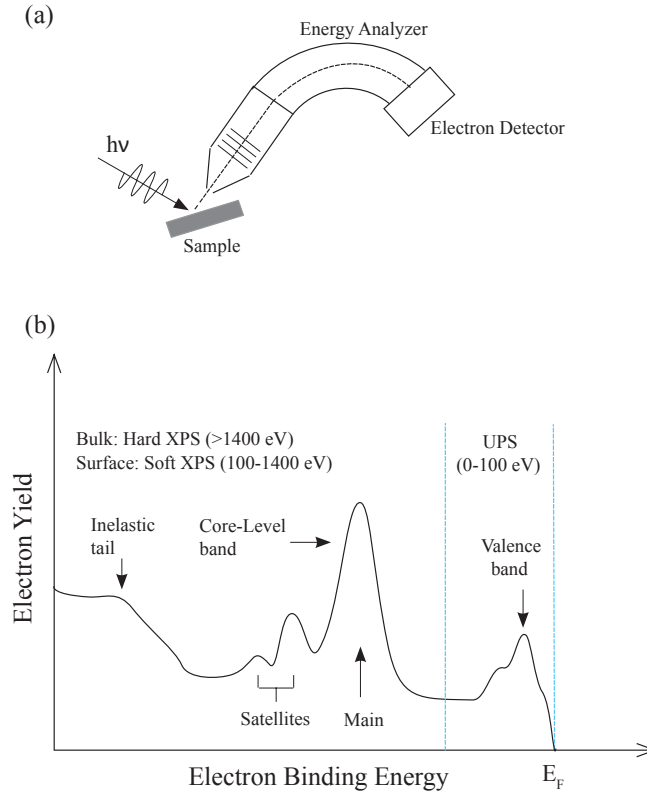


Figure 2.3: (a). Schematic picture of the XPS measurement system. (b) A schematic photoemission spectra produced by experiments.

2.2 Core-Level X-ray Photoemission Spectroscopy

2.2.1 Main lines and satellites

In x-ray photoemission spectroscopy (XPS), the electron is excited from the core level to above the Fermi energy by absorbing the energy of the monochromatic X-ray, and then escape out of the sample to vacuum where it is detected as a free electron (Fig.2.3). If the electrons in the system have no interaction with each other, the photoemission spectra would be the single lines distributed at different binding energies. Since the atoms,

2.2. Core-Level X-ray Photoemission Spectroscopy

molecules and solids we study in science are all many-electrons systems. The electrons in most of these systems always interact with each other via the coulomb and exchange interactions, and these interactions are responsible for the more complex line shape observed the PES spectra. The position of a peak is determined by the binding energy of the orbital having electron excitations, and each binding energy is corresponding to a particular element with a specified orbital and angular momentum. The width or the shape of the peak also plays an important role to reveal the correlations between electrons and the level of localization. Overall, one of the basic applications of the XPS is to detect the chemical information of the elements, and their orbital and spin properties in materials.

The removal of an electron by photoelectric effect leaves a core hole with a positive core hole potential U . This potential U can perturb the configuration of the remaining electrons and force them to reconstruct a new ground state, rather than keeping their original states as previously described by one-electron approximation. In a more complex view, the emission of one electron after the photoexcitation process can cause excitations in the remaining system. The energy delivered by these excitations to the sample must be gained from the kinetic energy of the outgoing electron. Therefore, we will detect an electron with a smaller kinetic energy than that expected. If we call the peaks in XPS spectra generated by the electrons without kinetic energy loss as the main line, then the electrons with a reduced kinetic energy could produce some additional peaks at the higher binding energy ($E_B = hv - E_{kin}$) compared to the main line, and we named them as satellites. Because these satellites are generated by the interactions between photoelectrons and the remaining system, they are inconsistent with the sudden approximation and thus are not easy to be described by a simple physical model. The other direct way to obtain the main line and satellites in the PES spectra is to consider the number of final states that can be reached after the photoexcitation. Main line is corresponding to the ground state; satellites appear only if more than one final states exist, and are corresponding to the excitation states which have already existed in the system before the photoemission process and generate additional peaks at low bind-

ing energy in PES spectra after the photoexcitation. These satellites can be well described by sudden approximation and are extremely useful for us to study the instabilities of the sample, in contrast to the undesired case of losing kinetic energy. Moreover, the possible ways to lose kinetic energy by the outgoing electrons are not limited to exciting other electrons, but can also include the inelastic collisions happened on their way escaping to the vacuum. The inelastic collisions usually exhaust a large portion of kinetic energy and will make the electrons form featureless broad peaks in the much higher binding energy region, which is named inelastic tail or secondary electrons, as illustrated in Fig.2.3. The emergence of satellites in the PE spectra is a very attractive phenomenon to understanding competing instabilities in correlated system, which are the results of the interplay in charge, spin, orbital and lattice degrees of freedom. However, the analysis of satellites is a complex matter, and only simple cases can be well described by the presently theoretical models, for example the Hubbard model and Anderson impurity model [Anderson, 1961].

2.2.2 Screening by the charge transfer

Although we have elaborated on the process of the core-level excitation in XPS, the purpose is not to study the core-level electronic structure, which is already known to be filled by following Hund's rule. We, however, use core-level excitations to obtain the information on the valence electrons, whose interactions give rise to a variety of interesting phases in the materials, such as MIT, giant magnetic resistance and superconductivity. To demonstrate how the core-level excitations reveal the valence states, we choose a simple example of copper dihalides with $3d^9L$ configuration, where $3d^9$ represents that the $3d$ orbital of Cu^{2+} is occupied by 9 electrons and 1 hole, and L refers to the highest occupied ligand shell such as $2p^6$ for O^{-2} . The energy of $3d$ orbital is usually higher than the highest energy of the ligand shell L . When one electron in the Cu $2p$ orbital is emitted by the photoexcitation, a core hole, in other words, a positive charge is created and consequently adds an additional coulomb potential U_{cd} into the system. This can be

perceived as the interactions between holes, here by referring to the core hole and the hole in $3d$ valence orbital. U_{cd} increases the hole potential, and inversely cause the energy of the $3d$ valence shell to decrease because there is an attraction between $2p$ core hole and $3d$ electrons. Consequently, the final states of electrons after the photoexcitation could have two possible ground states: (1) $\underline{c}3d^9L$, with \underline{c} representing that a $2p$ core hole exist. There is no configuration change in $3d$ electrons, because the lowered energy due to the emergence of U_{cd} is not enough to make a reconstruction of electrons configuration. (2) $\underline{c}3d^{10}\underline{L}$, with \underline{L} representing one hole in the ligand shell. When the effect of U_{cd} is strong enough, the much lowered energy of the $3d$ valence shell gets closer to, or even lower than, the highest energy in the ligand shell L . Now the configuration $\underline{c}3d^9L$ is an unstable state and the coulomb attraction between the core hole and electrons in the ligand shell will favorably transfer an electron from the ligand shell into the localized $3d$ orbital, in order to attain a new ground state $\underline{c}3d^{10}\underline{L}$ by overcoming the charge-transfer energy. The charge-transfer energy Δ is defined by $\Delta = E(d^{n+1}\underline{L}) - E(d^n L)$ to describe the energy cost to excite an electron from the ligand shell L to a d^n configuration of a metal ion. To quantitatively illustrate which final state is the ground state and which one is the satellite, a simple strategy is to compare the magnitude of U_{cd} and Δ . If $U_{cd} > \Delta$, the ground state is $d^{n+1}\underline{L}$ with a charge transfer, otherwise for $U_{cd} < \Delta$, the ground state is $d^n L$ without a charge transfer, as shown in Fig.2.4.

The phenomenon of a charge transfer in core-level photoemission is named as screening effect and was firstly verified in experiments on Ni metal by Hüfner and Wertheim in 1975 [Hüfner and Wertheim, 1975]. Since then, many attempts from theoretical approaches have been made and successfully provided a quantitative interpretation of the core-level photoemission spectra based on a charge-transfer model using an impurity-type configuration-interaction approach [Larsson, 1975; van der Laan et al., 1981; Zaanen et al., 1986; Park et al., 1988; Bocquet et al., 1992]. However, some important aspects are still not explained by these early interpretations, such as the large width of the main line of CuO and the high- T_c compounds [Fujimori et al.,

2.2. Core-Level X-ray Photoemission Spectroscopy

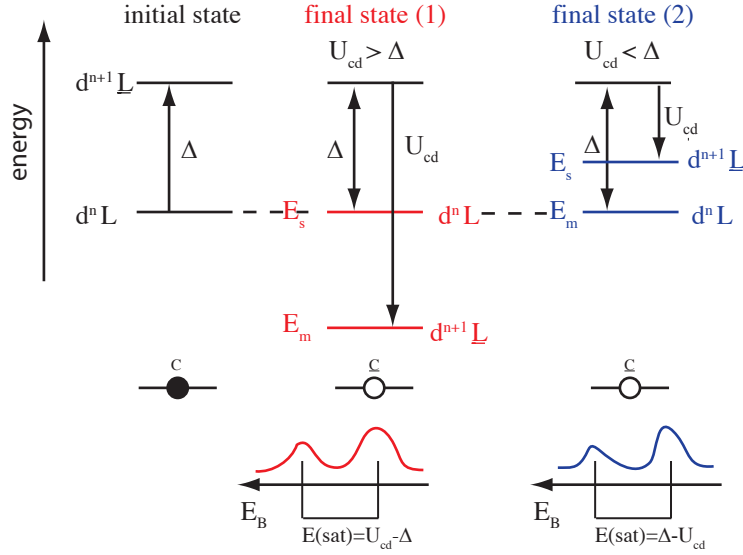


Figure 2.4: The schematic picture interprets the possible final ground state reached after a core-level photoemission in transition-metal compound under the assumption that there is no coupling between the metal and ligand ions [Hüfner, 1995]. Assuming that configurations $d^n L$ and $d^{n+1} L$ are two initial states and are separated by a energy gap Δ , The production of a core hole \underline{c} lows both energy level of two initial states, but $d^{n+1} L$ is lowered more than $d^n L$ for its one more $3d$ electron, and this lowering is described by U_{cd} . If $U_{cd} > \Delta$, the lowest final state is $d^{n+1} L$, otherwise $d^n L$ is the ground state for $U_{cd} < \Delta$. Under this approximation we can estimate that the main line-satellite separation is $|U_{cd} - \Delta|$.

1987; Shen et al., 1987] and the double-peaked structure of the main line of the Ni $2p$ XPS spectra of NiO, because the theories were restricted to the Anderson impurity limit, which is based on an assumption that screening is mainly achieved by electrons from the ligands surrounding the metal ion with a core-hole potential. In 1993, Veenendaal and Sawatzky discovered an additional screening channel strongly contributing to the Ni $2p$ and Cu $2p$ XPS spectra in NiO and CuO, respectively [Veenendaal and Sawatzky, 1993; Veenendaal et al., 1993]. This new screening channel, the non-local screening, goes beyond the Anderson impurity limit and involves the electrons

2.2. Core-Level X-ray Photoemission Spectroscopy

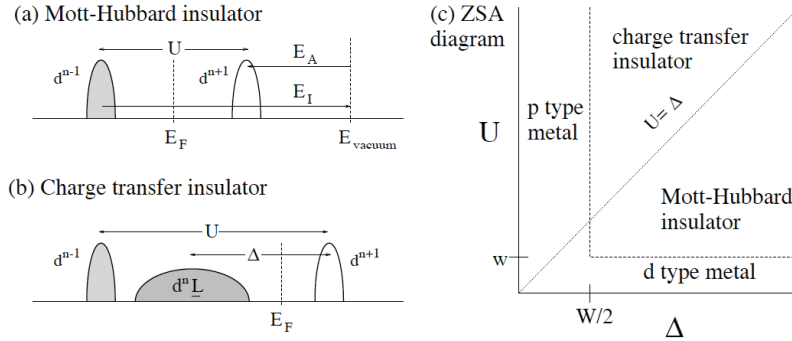


Figure 2.5: Schematic electron removal and addition states for a Mott-Hubbard insulator (a) and a charge transfer insulator (b). (c) The Zaanen-Sawatzky-Allen diagram for the various possible metallic and insulating situations encountered in transition metal compounds. [Pen, 1997]

transfer from ligands surrounding a neighboring metal site. For example in Fig.2.6, the final state in CuO due to the non-local screening is $\underline{c}3d^{10}$ in the Cu^{2+} site with a core hole plus a Zhang-Rice singlet with mainly $3d^9 \underline{L}$ character in the neighboring Cu^{2+} site [Zhang and Rice, 1988; Eskes and Sawatzky, 1988]. The lower energy of non-local screening state is related to the strong stabilization of the Zhang-Rice singlet band (ZRSB), so the non-local screening is called as "ZRSB screening" as well. The wide spread exist and the importance of non-local screening have been demonstrated by using larger clusters containing multi metal sites in cuprates and other transition metals [Veenendaal and Sawatzky, 1993; Veenendaal et al., 1993; Veenendaal, 2006; Okada, 2002, 2009].

2.2.3 The Zaanen-Sawatzky-Allen model

As described in the previous section, the phenomenon of a charge transfer occurs when the oxygen levels are higher than the lower Hubbard band (the occupied valence band of metal ions). However, if the oxygen levels are much lower than the lower Hubbard band, the charge transfer from the ligand shell would be prohibited and we call this kind of system as Mott-Hubbard system, such as the ruthnates oxides that we are studying in this

thesis. In Fig.2.5(a, b), it shows a schematic picture for these two types of insulating transition metal compounds. One of the differences between them should be noticed is the insulating gaps. The gap of the Mott-Hubbard insulator is determined by the excitations of the $d-d$ electrons and however, the gap for a charge-transfer insulator is determined by the charge transfer from the ligand band to metal ions. Therefore, if we add holes/electrons into the system either by chemically doping or in a photoemission/inverse photoemission experiment, the holes/electrons will go into the transition metal ions for the Mott-Hubbard insulator, while in the charge transfer insulator they enter the ligand shell (O-2*p* band).

The classification scheme for transition metal compounds has been proposed by Zaanen, Sawatzky and Allen [Zaanen et al., 1985] based on the on-site Coulomb interaction U and the charge transfer energy Δ , shown in Fig.2.5(c). The on-site Coulomb interaction U , for an open 3*d* (4*d*) shell, is the repulsion energy of two electrons occupying the same 3*d* (4*d*) orbital, and can be defined as the energy cost for removing an electron from a d orbital and putting it in another d orbital on a site far away. Considering two d^n ions, the removal and addition of an electron would produce a d^{n+1} and a d^{n-1} configuration, respectively, and the energy difference between initial states and final states are the on-site Coulomb interaction, which is $U = 2E(d^n) - E(d^{n+1}) - E(d^{n-1})$ with neglecting the hybridization.

In the Zaanen-Sawatzky-Allen (ZSA) classification scheme, the transition metal compounds can be divided into four groups by the two parameter U and Δ , together with the band widths of the d band (w) and of the p band (W), which are determined by the hybridization in the transition metal ions and in ligand shell. Because the $d_i^{n-1}d_j^{n+1}$ excited states will have a band dispersion width $2w$, and the $d_{n+1}\bar{L}$ states have a band dispersion width $w + W$, for $U > w/2$ and $\Delta > (w + W)/2$, the material is either a charge transfer ($U > \Delta$) or a Mott-Hubbard ($U < \Delta$) insulator. When the hybridization increases ($U < w/2$ and $\Delta < (w + W)/2$), the materials will go through an insulator-metal transition and become a d or p type metal, depending on the relative magnitude to U and Δ .

2.2.4 Cluster model

The cluster model is the general theoretical method to interpret features of XPS spectra by numerical diagonalization calculations. It is a charge-transfer model using an impurity-type configuration-interaction Hamiltonian, which consists a core-hole potential term, on-site coulomb repulsions and interactions between metal ions and ligand shell. Here we still take the cuprates as an example as shown in Fig.2.6, the Hamiltonian for the core-level spectroscopies is [Okada, 2009]:

$$H = H_{dp} + H_{core}, \quad (2.5)$$

The H_{dp} is the Hamiltonian describing the valence hole system and is written in the hole picture as:

$$\begin{aligned} H_{dp} = & \sum_{i,\sigma} \varepsilon_d n_{d,i\sigma} + \sum_{j,\sigma} \varepsilon_p n_{p,j\sigma} \\ & + \sum_{\langle i,j \rangle, \sigma} V_{pd,ij} (d_{i\sigma}^\dagger p_{j\sigma} + p_{j\sigma}^\dagger d_{i\sigma}) \\ & + \sum_{\langle j,j' \rangle, \sigma} V_{pp,jj'} (p_{j\sigma}^\dagger p_{j'\sigma} + p_{j'\sigma}^\dagger p_{j\sigma}) \\ & + \sum_i U_{dd} n_{d,i\uparrow} n_{d,i\downarrow} + \sum_j U_{pp} n_{p,j\uparrow} n_{p,j\downarrow} \\ & + \sum_{\langle i,j \rangle, \sigma, \sigma'} U_{dp} n_{d,i\sigma} n_{p,j\sigma'}, \end{aligned} \quad (2.6)$$

where d_{is}^\dagger (p_{js}^\dagger) creates a hole on the i -th Cu $3d_{x^2-y^2}$ orbital (the j -th O $2p$ orbital), and σ (σ') takes \uparrow or \downarrow . The first and second terms on the right hand side of eq.(2.6) are the single-particle energies where $n_{d,is}$ ($n_{p,is}$) is the number operators for the Cu $3d$ (O $2p$) holes. The third term refers to hybridization between the Cu $3d$ and O $2p$ orbitals, where $\langle i, j \rangle$ denotes the summations over the nearest-neighbor pairs. The fourth term represents the hybridization between neighboring O $2p$ orbitals. The fifth and sixth terms represent the on-site coulomb interaction in Cu $3d$ and O $2p$ orbitals,

2.2. Core-Level X-ray Photoemission Spectroscopy

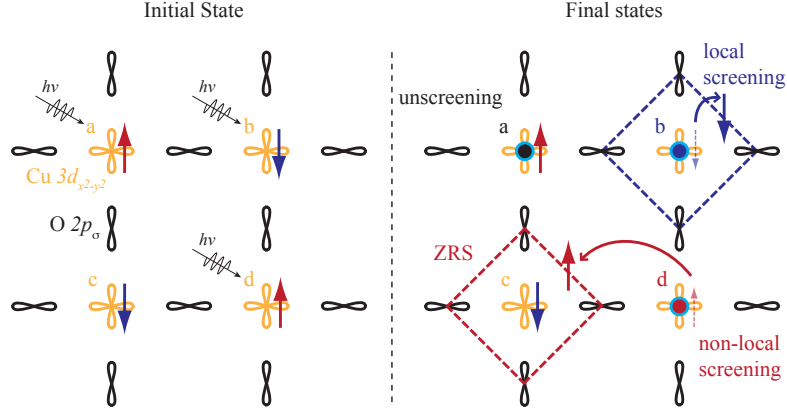


Figure 2.6: Schematic illustrations for the initial state and the final states induced in XPS in cuprates. (Left) The initial ground state $3d^9L$ in the cuprates with on average one hole indicated by the arrows per CuO_4 plaquette. Shown are the $\text{Cu } 3d_{x^2-y^2}$ orbitals for the copper and the σ -bonding $2p$ orbitals of the oxygen. (Right) The possible XPS final states when a core $2p$ electron in each (a,b,d) sites is removed, where the core hole indicated by an circle with a blue outline. Site (a) is the unscreened final state $\underline{c}3d^9L$. In site (b) an electron transfers in from the oxygens surrounding the site b with a core hole and forms a local screening on the core hole, and the configuration is $\underline{c}3d^{10}\underline{L}$. In site (d) an electron moves from the neighboring site (c) to site (d) to screen the core hole, which is known as non-local screening $\underline{c}3d^{10}\underline{L}$. In site (c) the oxygen obtain an additional hole, and it forms a configuration $3d^9\underline{L}$, which called Zhang-Rice singlet (ZRS).

respectively. The last term represents the nearest-neighbor Cu-O repulsions.

The H_{core} is to describe the interaction induced by the Cu $2p$ core hole after the photoexcitation:

$$\begin{aligned}
 H_{core} = & \sum_i \varepsilon_{\text{Cu}2p} n_{\text{Cu}2p,i\sigma} + \sum_j \varepsilon_{\text{O}1s} n_{\text{O}1s,j\sigma} \\
 & + Q_{\text{Cu}2p} \sum_{i,\sigma,\sigma'} n_{d,i\sigma} n_{\text{Cu}2p,i\sigma'}, \quad (2.7)
 \end{aligned}$$

where the first and second terms on the right hand side of eq.(2.7) repre-

sents the Cu $2p$ and O $1s$ one-body atomic states, respectively. The third term represents the Cu $2p$ – Cu $3d$ Coulomb repulsion, respectively. $Q_{\text{Cu}2p}$ describes the Coulomb repulsion between core hole and $3d$ holes as the U_{cd} we have mentioned before.

For the Mott-Hubbard system, we can easily obtain the Hamiltonian by removing the terms with contributions from oxygens in eq.(2.6) and eq.(2.7). The charge transfer (CT) energy (Δ) is defined by $\Delta = \varepsilon_p - \varepsilon_d$ for cuprates and $\Delta = \varepsilon_p - \varepsilon_d - U_{dd}$ for cases with more than one hole in the valence orbital, such as Ruthenates. In a restrictive way, the Oxygen $2p$ have a bandwidth W_p , so the energy cost for transferring an electron from O site to Cu site should be $\Delta - W_p$. Using the numerical ways such as the Lanczos method, the Hamiltonian of eq.(2.5) is diagonalized to obtain the eigenstates and eigenvalues as energy in the system. The photoemission spectra $I(E_B)$ is then calculated by using eq.(2.3).

2.3 Angle-Resolved Photoemission Spectroscopy

Angle-resolved photoemission spectroscopy (ARPES) is a momentum determined, low-energy electron excitation measurement which has been widely applied to investigate correlated systems, especially with a great success in high- T_c superconductors [Damascelli et al., 2003]. During an experiment, a low-energy beam of the monochromatized radiation, which is generated by a gas-discharged lamp, laser or a synchrotron beamline, is used to illuminate the sample to emit electrons by the photoelectric effect. The emitted electrons, named photoelectrons, travel to the sample surface in the solid and eventually escape into the vacuum, as described by the three-step model in section 2.1. In the vacuum, the emitted photoelectrons are detected by an electron-energy analyzer and both their kinetic energy and emission angles are measured. Thus the momentum of a photoelectron \mathbf{p} in vacuum can be determined by $p = \sqrt{2mE_{kin}}$ together with its polar (ϑ) and azimuthal (φ) emission angles. In the solid, the total energy and momentum conservation laws can be applied to the system of crystal and photoelectron during

2.3. Angle-Resolved Photoemission Spectroscopy

the photoexcitation process. The fact of a very short electron escape length allows us to reasonably assume that there are no interactions between the photoelectron and the remaining electrons. When the photoelectron arrives the surface, it has to consume a portion of kinetic energy to overcome the perpendicular surface potential before escaping into the vacuum. Thus, the perpendicular component of momentum is not conserved, but the parallel component is still conserved:

$$\mathbf{p}_{||} = \hbar \mathbf{K}_{||} = \sqrt{2mE_{kin}} \cdot \sin\vartheta. \quad (2.8)$$

where the \mathbf{K} is the momentum of the photoelectron inside the solid with the sample surface assumed to be in xy plane. By scanning the energy and momentum distribution of photoelectrons in real space, ARPES data provides a vivid picture to directly observe the Fermi surface (FS) and band structure in the solid. To associate the measured parameters with band structure, we firstly write down the general expression of momentum both in the angular space and \mathbf{k} space:

$$\begin{aligned} \mathbf{K} &= \frac{1}{\hbar} \sqrt{2mE_{kin}} (\cos\varphi \sin\vartheta \hat{i} + \sin\varphi \sin\vartheta \hat{j} + \cos\vartheta \hat{k}) \\ &= \mathbf{K}_x + \mathbf{K}_y + \mathbf{K}_z \\ &= \mathbf{k}_x + \mathbf{k}_y + \mathbf{k}_z + \mathbf{G}. \end{aligned} \quad (2.9)$$

where the small \mathbf{k} is the wave vector of a Bloch state in the Brillouin zone (BZ) and \mathbf{G} is a Bravais lattice vector. The polar angle ϑ and azimuthal angle φ are used in the normal sphere coordinates. Therefore, the band structure can be obtained by plotting the intensity distribution of electrons in a binding energy and momentum plane. Considering that only the component of momentum parallel to the sample surface is conserved, a general ARPES measurement is not available to provide a three-dimensional (3D) band structure, although some experimental methods have been developed to obtain a 3D band mapping [Hüfner, 1995; Stroscov et al., 1997, 1998]. We note that the relationship in equation (2.9) is correct only in the plane of sample surface.

2.3. Angle-Resolved Photoemission Spectroscopy

Low energy of the incoming photons in ARPES is needed to obtain a high energy and momentum resolution, which is easy to see by looking at the momentum differential $\Delta\mathbf{K}$ from eq.(2.8):

$$\Delta\mathbf{K}_{\parallel} \simeq \sqrt{2mE_{kin}/\hbar^2} \cdot \cos\vartheta \cdot \Delta\vartheta. \quad (2.10)$$

In eq.(2.10), a contribution from a fine energy resolution ΔE_{kin} is neglected and it clearly shows that either using lower photon energy or detecting electrons with a larger emission angle ϑ would improve the momentum resolution. The lower photon energy also brings another benefit of an easier achievement of a higher energy resolution. However, the drawback of working at low photon energies is the extreme surface sensitivity due to the associated short mean free path for the unscattered photoelectrons (5Å for 20-100 eV kinetic energy). The surface sensitivity thus limits the application of ARPES on bulk properties investigation and requires an atomically clear sample surface and an ultra-high vacuum condition (lower than 5×10^{-11} torr), with a much higher standard even in comparison with the XPS working environment.

The establishment of a theoretical expression for the ARPES spectra under three-step model and sudden approximation is beyond the scope of this thesis and its detailed description can be referred to Damascelli's papers [Damascelli et al., 2003; Damascelli, 2004] and references therein. Here, we would rather focus on the analysis of ARPES experimental data on the Mn doped $\text{Sr}_3\text{Ru}_2\text{O}_7$, such as fermi surface (FS), energy and momentum distribution curves in term of doping levels of Mn impurities and temperature, in order to reveal the band structures and link them to the principle of a MIT.

Chapter 3

Suppressed Screening Channel in $\text{Sr}_3(\text{Ru}_{1-x}\text{Mn}_x)\text{O}_7$ by Substitutional Mn doping

3.1 Introduction

Chemical doping, i.e. the change of carrier density in a material, is one of the most commonly used techniques to tailor novel properties in strongly correlated systems. Transition metal oxides (TMO) are paradigmatic in this sense: they often display several rather different electronic phases that are quite close in energy, and the equilibrium state eventually reached is decided by minute changes in parameter space, such as the effect obtained by impurity doping. Knowing that the main obstacle to obtain a comprehensive description of TMO is to disentangle the different, but comparable, energy scales, research on the Ruddlesden-Popper (RP) $(\text{Sr,Ca})_{n+1}\text{Ru}_n\text{O}_{3n+1}$ series (crystal structures shown in Fig.1.1) which shows rich phase competitions such as from superconductor to Mott insulator and from paramagnet to anti-ferromagnet, has recently suggested a conceptually different approach, based on substitutional doping. One of the central features in the rich physics of RP compounds is the extension of 4d orbitals: ground state properties of ruthenates are extremely sensitive to orbital degrees of freedom, i.e. to both the angle and the length of the Ru-O bonds, resulting in almost equal chance of displaying itinerant or localized behaviour. It is therefore clear how substitution of Ru 4d with more localized 3d metal atoms, i.e. with a smaller ionic radius, will strongly influence orbital population, and more

3.2. Experiment

generally the interplay between charge, spin and orbital degree of freedom, possibly resulting in orbital-induced novel properties. Examples of this approach is the use of Chromium (Cr^{4+}) in $\text{CaRu}_{1-x}\text{Cr}_x\text{O}_3$ [Durairaj et al., 2006] and $\text{SrRu}_{1-x}\text{Cr}_x\text{O}_3$ to stabilize itinerant ferromagnetism from the normal paramagnetic state [Pi et al., 2002; Klein et al., 2006; Williams et al., 2006]. In general, Cr, Ti, and Rh substitution produce a large spectrum of magnetic properties, evolving from antiferromagnetism to ferromagnetism, via the metamagnetism and spin density wave behavior of the pure and Ti-doped systems [Grigera et al., 2004b,a]. More recently, a 5% substitution of Mn for Ru in the bilayered member $\text{Sr}_3\text{Ru}_2\text{O}_7$ has been shown to change the ground state from a paramagnetic metal to an antiferromagnetic insulator with an unexpected zig-zag magnetic superstructure accompanied by a long-range orbital order (Fig.3.1) [Mathieu et al., 2005]. Furthermore, the interplay between anisotropic Ru 4d-O 2p bond and the localized Mn 3d impurity is responsible of the observed crystal field level inversion, with Mn acting as an Mn^{3+} acceptor instead of the expected Mn^{4+} valence [Hossain et al., 2008] as shown in Fig.3.2, a behavior bearing interesting similarities with Mn doped GaAs in dilute magnetic semiconductors. Unraveling what ultimately drives the electronic and magnetic properties of the doped $\text{Sr}_3(\text{Ru}_{1-x}\text{Mn}_x)_2\text{O}_7$ system is strictly linked to a direct measure of the electronic charge distribution over Ru and O orbitals, together with the hybridization strength within the RuO plaquette. PES possesses all the necessary characteristics in elucidating the abovementioned rich physics. In particular, core level PES is sensitive to the different screening channels, the energy location and the relative ratio of specific peaks, in a chemical selective way. Therefore, we hope to follow the MIT in the evolution of the well screened and poorly screened picture in terms of Mn doping.

3.2 Experiment

The $\text{Sr}_3(\text{Ru}_{1-x}\text{Mn}_x)_2\text{O}_7$ samples ($x = 0.05, 0.1, 0.2$) we used are the ultra-clean single crystals most recently grown by our collaborators in the groups led by Y. Yoshida (at AIST in Tsukuba), H. Takagi and Y. Tokura (Uni-

3.2. Experiment

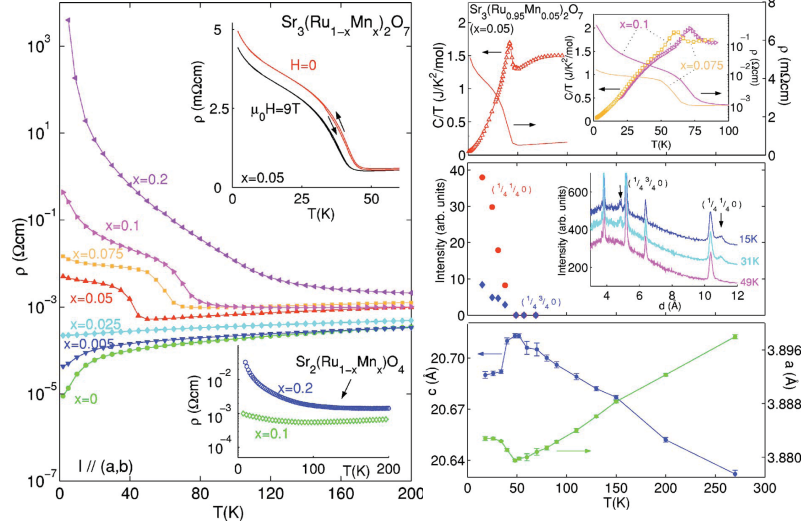


Figure 3.1: Transport measurements of $\text{Sr}_3(\text{Ru}_{1-x}\text{Mn}_x)_2\text{O}_7$ after Mathieu *et al.* [Mathieu *et al.*, 2005]. Temperature dependence of the resistivity ρ for different Mn doping x shows a metal-insulator transition occurs with $x \geq 0.05$. The intensity of the $(1/4, 1/4, 0)$ and $(1/4, 3/4, 0)$ magnetic peaks were observed in neutron diffractograms as shown in the middle panel of the right hand side, which indicates a long-rang magnetic ordering introduced by Mn doping.

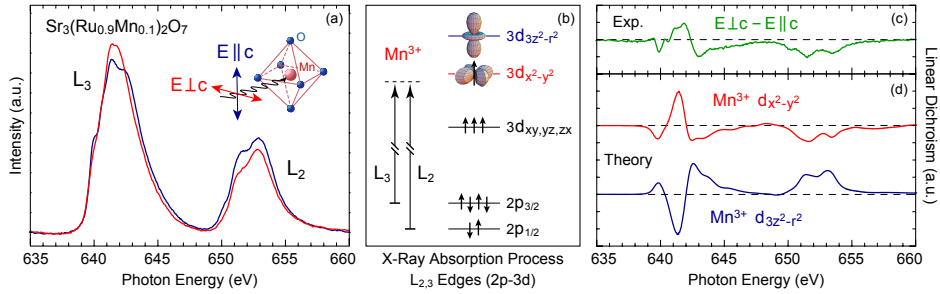


Figure 3.2: Linear Dichroism (LD) Mn $L_{2,3}$ –edge X-ray absorption spectra from $\text{Sr}_3(\text{Ru}_{0.9}\text{Mn}_{0.1})_2\text{O}_7$ at $T = 295\text{K}$ and the corresponding multiplet cluster calculations after M. A. Hossain *et al.* [Hossain *et al.*, 2008], which shows Mn^{3+} has an unusual crystal-field level inversion.

3.3. Results and Discussion

versity of Tokyo). These crystals exhibit superior quality, as evidenced by the low residual resistivity in zero field [Mathieu et al., 2005]. PES measurements were performed using two experimental setups: the advanced photoelectric-effect experiments (APE) beamline for low energy PES [Panaccione et al., 2009] (Elettra, Trieste - base vacuum 1×10^{-10} mbar) and VOLPE spectrometer [Torelli et al., 2005] for hard x-ray PES (HAXPES) (beamline ID16 at European Synchrotron Radiation Facility ESRF, base vacuum 6×10^{-10} mbar). The spot size at normal emission geometry was $50 \times 120 \mu\text{m}^2$ in both cases and the overall energy resolution (beamline + analyser) was set to 450 meV (VOLPE) and 200 meV (APE). The position of Fermi energy E_f and the overall energy resolution were estimated by measuring the metallic Fermi edge of polycrystalline Au foil in thermal and electric contact with the samples. When not specified otherwise, we present data obtained on samples fractured in UHV. Identical results have been obtained consistently on several cleaved samples. For the measurements carried out at APE, the cleanliness of the surface has been checked by the measure of C 1s and O 1s spectra. Surfaces are very sensitive to contaminations, resulting in an average measurement time of 4 hours before a new cleavage is needed. No traces of contamination were observed, over two days and at any temperature, in HAXPES measurements.

3.3 Results and Discussion

In this chapter, we present PES data from $\text{Sr}_3(\text{Ru}_{1-x}\text{Mn}_x)_2\text{O}_7$ ($x = 0.05, 0.1, 0.2$), where we monitor the evolution of Ru 3d fine structure vs. Mn-doping, temperature and depth. In both Ru $3d_{3/2}$ and Ru $3d_{5/2}$, a clear suppression of the metallic features (well screened satellite peaks) is observed, implying, already at low doping, a sharp transition from itinerant to localized character. Comparison between soft and hard x-ray PES, hence tunable depth sensitivity, reveals that the degree of localized-metallic character is different at the surface and in the bulk of the material. Analysis of the intensity ratio and binding energy position of the Ru 3d core level and satellites give reliable estimate of both charge transfer energy and number of holes for Ru

3.3. Results and Discussion

site. Our results suggest a way to control, in the same material, metallicity of the surface-interface region vs. the bulk one, by exploiting the highly sensitive response of conducting perovskites to impurities.

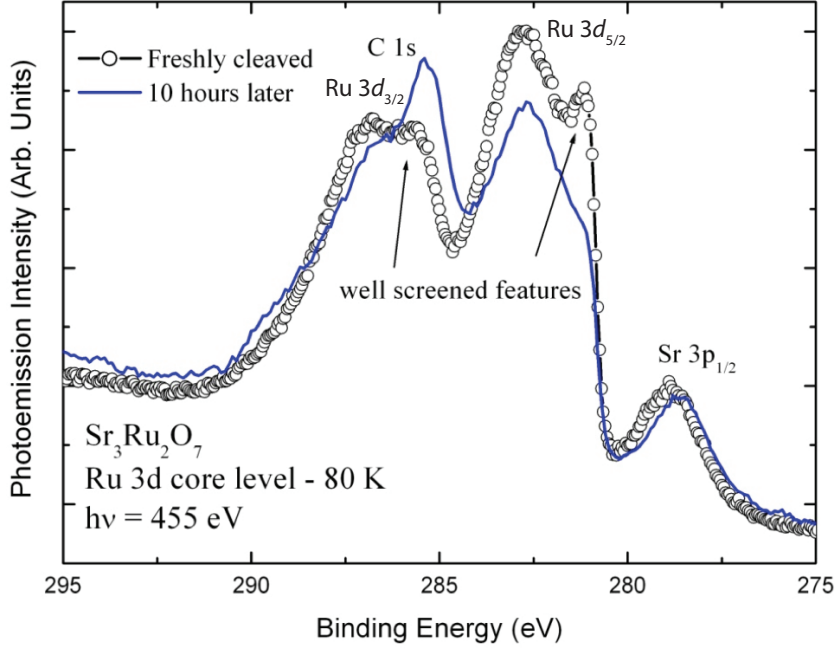


Figure 3.3: Ru 3d photoemission spectra of $\text{Sr}_3\text{Ru}_2\text{O}_7$ measured with $h\nu=455\text{eV}$ at 80 K. Beside the unscreened main peaks, the well screened peaks are seen at low binding energy side of both $\text{Ru}3d_{3/2}$ and $\text{Ru}3d_{5/2}$. The strong age effect of the sample is shown by blue line, which is measured 10 hours after the sample cleaved, and the well screened peaks are strongly suppressed by the contaminants.

3.3.1 APE spectra

Surface sensitive ($h\nu = 455\text{eV}$) Ru 3d core level spectra of $\text{Sr}_3\text{Ru}_{(1-x)\text{Mn}_x}\text{O}_7$ with $x = 0, 0.05$ and 0.2 are presented in Fig.3.3 and Fig.3.4. We identify the Sr $3p_{1/2}$ peak at about 279 eV of binding energy (BE) and the Ru spin-orbit split doublet $3d_{5/2}$ and $3d_{3/2}$ peaks in the energy window of 280-295 eV of

3.3. Results and Discussion

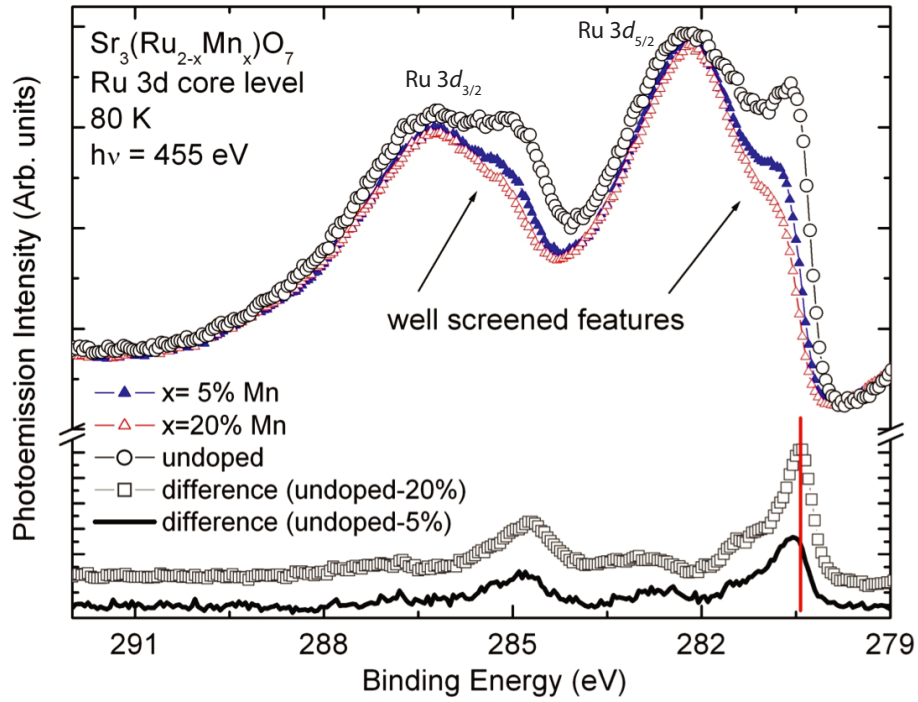


Figure 3.4: Mn doping dependence of Ru 3d photoemission spectra in $\text{Sr}_3\text{Ru}_{1-x}\text{Mn}_x\text{O}_7$. With the Mn concentration increasing, the well screened features become gradually absent due to the MIT in the sample.

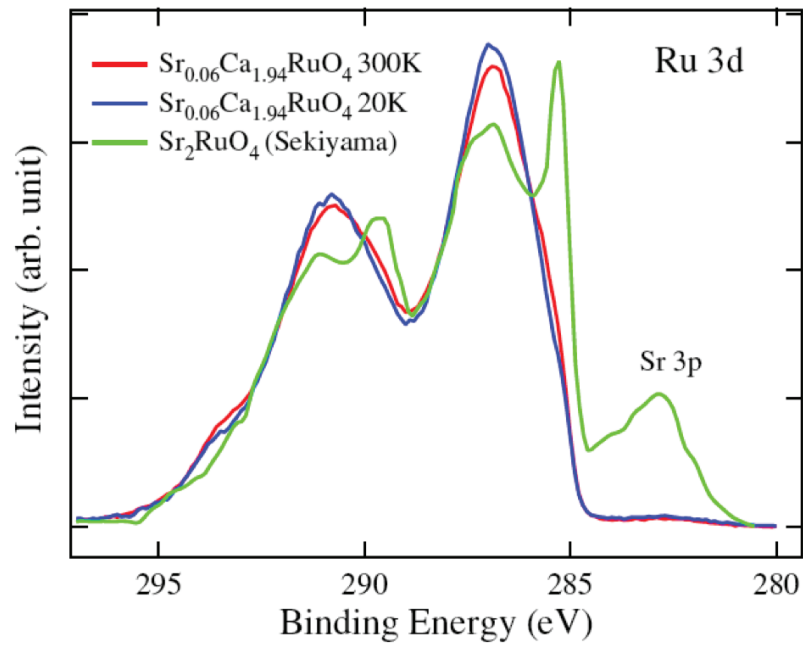


Figure 3.5: Ru 3d photoemission spectra of Sr_{0.06}Ca_{1.94}RuO₄ and Sr₂RuO₄ from Han-Jin Noh's PhD thesis [Noh, 2003].

3.3. Results and Discussion

BE . Looking at the $\text{Sr}_3\text{Ru}_2\text{O}_7$ parent compound spectrum one can easily decipher multiple components associated with Ru $3d$ doublet. Satellites at the low BE side, labeled as shake down features or well screened peaks, have been already observed in the ruthenate family. It is generally agreed that: i) features are not induced by surface-related chemical states, and ii) their spectral weight increases when the system enters a metallic regime [Takizawa et al., 2005; Kim et al., 2004; Sekiyama et al., 2004a]. Figure.3.3 reports the evolution of the spectral lineshape as a function of time in pure $\text{Sr}_3\text{Ru}_2\text{O}_7$: well screened features of Ru $3d$ core level are well resolved in freshly cleaved surfaces, whereas contaminated surfaces display intense C $1s$ structures at ~ 285 eV BE, resulting in a non statistical branching ratio between Ru $3d_{5/2}$ and $3d_{3/2}$. Interestingly, the presence of contaminants on the surface leads to a suppression of the well screened peaks, together with the appearance of a shoulder at 288 eV BE. Important changes are observed as a function of Mn doping (Fig.3.4): the intense well screened features, at the low binding energy side of both Ru $3d_{5/2}$ and $3d_{3/2}$, are severely suppressed already for $x=5\%$ Mn content, resulting only in a weak shoulder for $x=20\%$. It is interesting to note that both Mn 5% and 20% doped spectra display close similarities with Ru $3d$ core level in $(\text{Sr}_{1-x}\text{Ca}_x)_2\text{RuO}_4$, which is the system can undergo from the superconductor to the antiferromagnetic insulator with Ca doping. As illustrated in Fig.3.5, both unscreened and screened peaks can be well defined in metal SrRuO_4 but only unscreened peaks appear in the insulator system $\text{Sr}_{0.06}\text{Ca}_{1.94}\text{RuO}_4$, in comparison with Sr_2RuO_4 . Knowing that the a MIT upon doping has been reported in $\text{Sr}_3(\text{Ru}_{1-x}\text{Mn}_x)_2\text{O}_7$ [Mathieu et al., 2005; Hossain et al., 2008], we argue that present results hold the direct evidence of an electronic driven transition, via the observed evolution of the well screened satellites. The difference spectra in the bottom of Fig.3.4 highlight the transfer of spectral weight upon doping. A energy shift up to $\simeq 100$ meV for 20% Mn,(as indicated by the red line) of the $3d_{3/2}$ well screened features vs. Mn doping is observed. Moreover, the lineshape of the difference spectra reveal a fine structure of the satellites, with sizeable intensities around 281 eV and 285 eV of BE, and clear shoulders at the high BE side of each spin orbit partner (centered at 285.4 eV and 282.4 ev BE).

3.3.2 VOLPE spectra

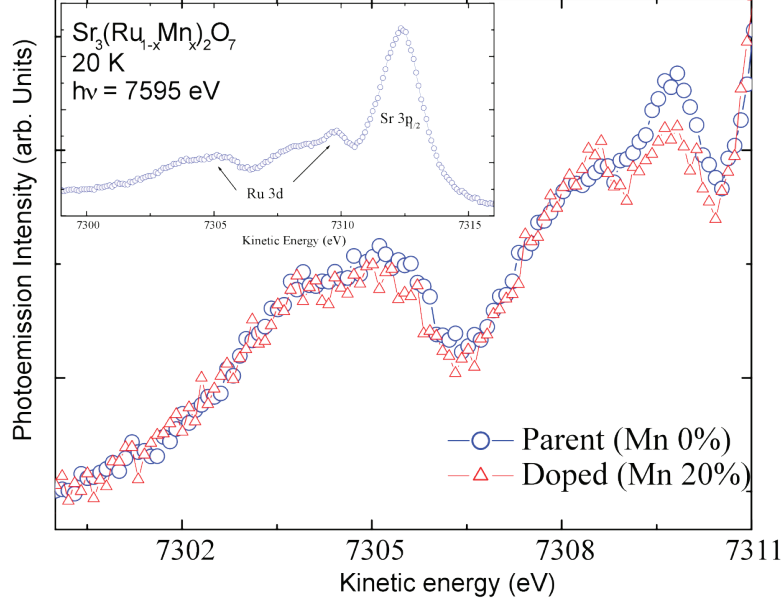


Figure 3.6: Ru $3d$ HAXPES spectra in $\text{Sr}_3\text{Ru}_{(1-x)}\text{Mn}_x)_2\text{O}_7$ with $x = 0$ and 0.2 with $h\nu=7959\text{eV}$ at 20 K .

The extreme sensitivity of the well screened features, and hence of the available screening channels, to the local environment, calls for a more accurate determination of the metallic-insulating character upon doping. To this goal, in Fig.3.6 we report HAXPES results, where bulk sensitivity $> 8\text{ nm}$ is guaranteed. The reduced influence of surface condition on the PES spectra is confirmed by the lineshape of Sr $3d$ core level measured in the HAXPES regime (Fig.3.7): the presence of a single component in both spin orbit partners is the signature of almost pure bulk signal, in agreement with previous results [Sekiyama et al., 2004b]. In Fig.3.6, one notices that the relative ratio between Sr and Ru peaks is significantly different between low energy PES and HAXPES data, as due from the different p/d cross section ratio when passing from soft to hard x-ray [Panaccione et al., 2005]. Zooming on the Ru $3d$ region, well screened peaks are observed at the same BE and with

3.3. Results and Discussion

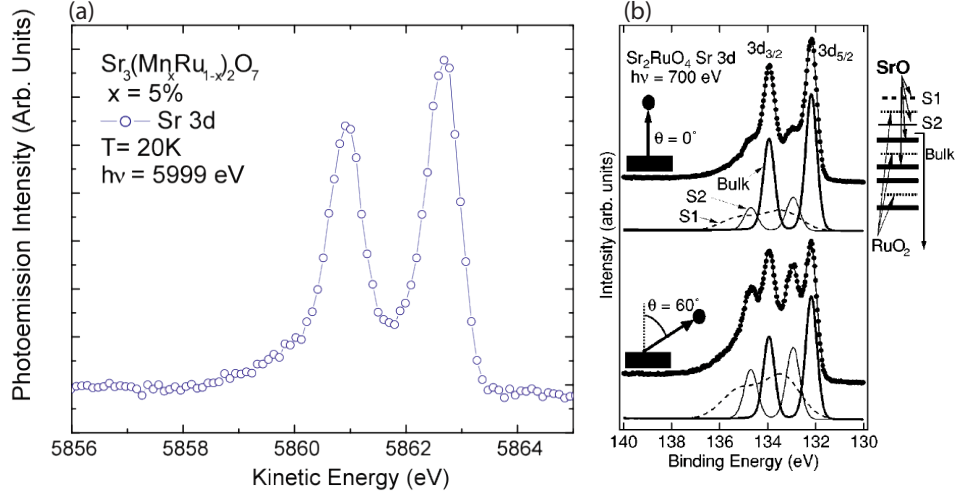


Figure 3.7: (a) Sr $3d$ HAXPES spectra in $\text{Sr}_3\text{Ru}_{(0.95}\text{Mn}_{0.05})_2\text{O}_7$ with $h\nu=5999$ eV at 20 K. The single component in both Sr $3d_{3/2}$ and $3d_{5/2}$ peaks indicates the spectra only with bulk signals. (b) Sr $3d$ core-level photoemission spectra for Sr_2RuO_4 . The spectra are well deconvoluted into contributions from bulk and surface layers (indicated by S1 and S2) [Sekiyama et al., 2004b].

same energy separation with respect to the low energy results. Although the evolution as a function of Mn doping is confirmed, it is evident that the relative ratio between main peak and well screened features is now reversed with respect to surface sensitive results. Based on the enhanced probing depth of HAXPES [Sacchi et al., 2005], the increase of well screened peaks in the hard x-ray regime have been recently explained in $3d$ -based TMO as the result of significant changes in the screening mechanism between surface and volume [Taguchi et al., 2005; Horiba et al., 2004]. HAXPES results in vanadates across the metal insulator transition also confirm the relationship between well screened satellites and metallicity [Panaccione et al., 2006].

3.3.3 Fitting of the spectra

To better disentangle well screened and poorly screened features and also to identify any additional components, we performed a spectral decomposition by fitting routines: results are presented in Fig.3.8 and 3.9. Each peak was represented by a symmetric function generated by a Lorentzian function convoluted with a Gaussian. The Lorentzian function represents the life time broadening effect, while the Gaussian function accounts for all other broadenings including energy resolution. A Shirley-type experimental background which is assumed to be proportional to the area under the photoemission signal is also included. The spectra recorded using 455 eV incident energy could be best fitted using one such function alone with three sets of doublets, one doublet for the main Ru 3d spin-orbit split peaks (black curves), one for the satellite feature appearing at the lower binding energy side (non-local screened peaks, red curves) and the third for the satellite features appearing at the higher binding energy side (unscreened peaks, blue curves) with the intensity ratio between the spin-orbit split components being fixed at 1.5, determined by the degeneracy ratio. For the bulk sensitive spectra recorded using 7995 eV photon energy, spectral decomposition resulted in only two sets of doublets, one corresponding to the main Ru 3d spin-orbit split peaks and the other corresponding to the non-local screened peaks. Within the error bar, unscreened peaks are absent (or with negligible intensity). Such reduction of unscreened peak intensity may be a further confirmation of a different itinerant-localized character when passing from the surface to bulk. Results of spectral decompositions are summarized in Table 3.1, where we observe: the ratio between well screened and main peak is almost identical

Table 3.1: Compound ratio of well screened/main peak intensity

peak	Undoped (APE)	Mn 20% doped (APE)	Undoped (VOLPE)	Mn 20% doped (VOLPE)
Ru $3d_{3/2}$	0.22	0.15	0.57	0.51
Ru $3d_{5/2}$	0.23	0.15	0.58	0.50

for both spin-orbit splitting peaks in the APE (surface sensitive) results.

As visible in Fig.3.3 and 3.4, the analysis of the peaks gives reliable results in the intensity (area) estimate, but the quality of the fit, constrained to statistical ratio, results to be less reliable in energy position of the peaks. Forcing the fitting procedure to obtain the best fit and allowing non statistical ratio+ further components, the energy location of the peaks could be identified with better precision. The reliability of the fit increases, residuals decreases (perfectly normal if we allow the presence of further components). One observes the presence of extra contribution, with lineshape similar to the well screened peaks (single red component in Fig.3.10). This extra contribution is similar (both in energy location and shape) to the one proposed by Sekiyama et al. [Sekiyama et al., 2004b], where the presence of a so-called “subsurface” contribution is proposed. Energy splitting between well screened peaks and main peaks are the same, within error bars, in both HAXPES and low energy spectra. Moreover, analysis confirm a decrease of the splitting when Mn content increases (from 1.50 ± 0.1 eV nondoped to 1.3 ± 0.1 eV Mn20% doped). Obviously, non statistical ratio is a very crude, and almost unphysical approach, while energy position of the peak can be directly extracted from the experimental data.

3.3. Results and Discussion

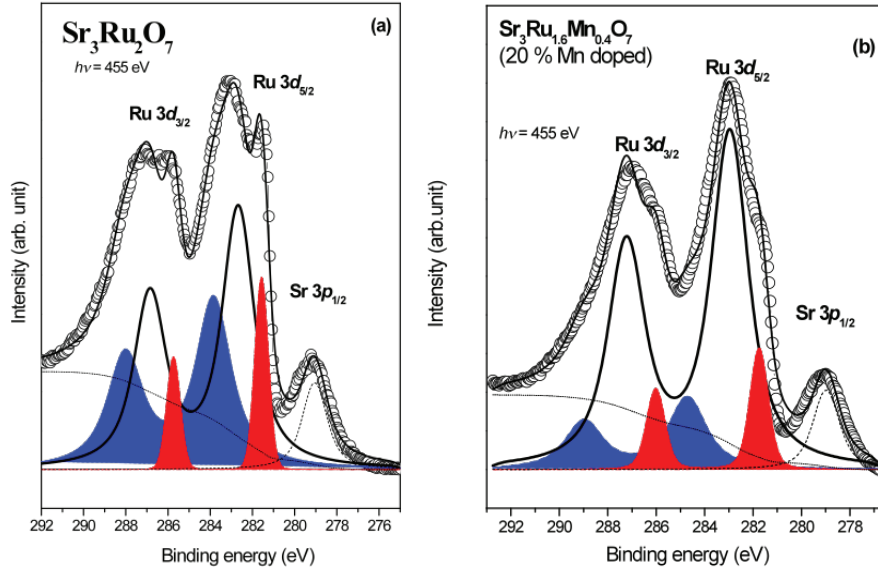


Figure 3.8: Analysis of relative intensity and energy position of Ru $3d$ peaks in APE. The fitting curves with red, black and blue colors are corresponding to the non-local screened, main and unscreened peaks, respectively.

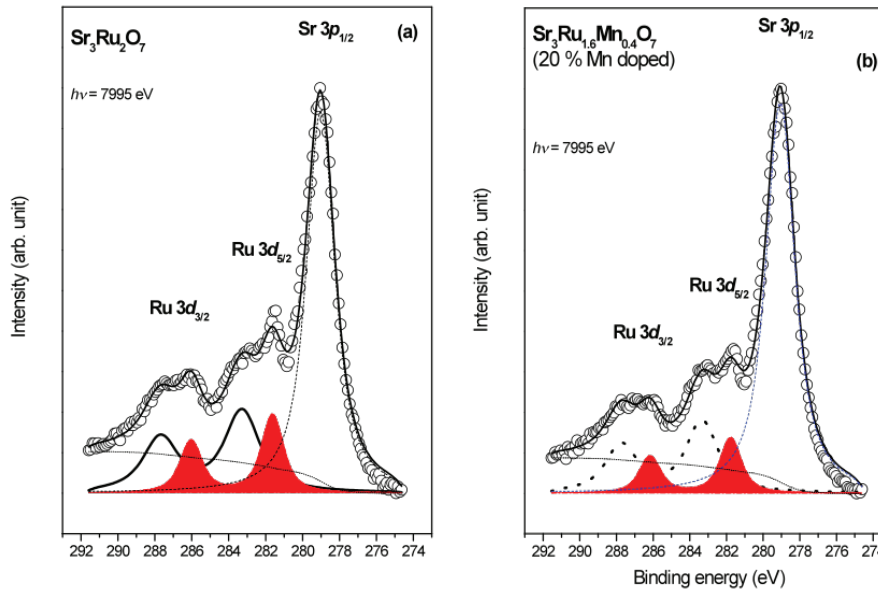


Figure 3.9: Analysis of relative intensity and energy position of Ru $3d$ peaks in HAXPES.

3.3. Results and Discussion

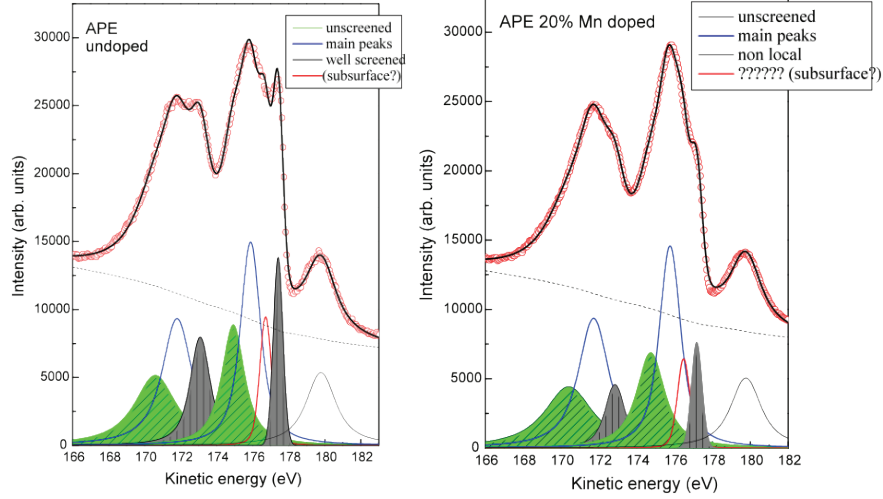


Figure 3.10: Best fit for APE Ru 3d spectra. The subsurface contribution was shown by a single red component.

3.3.4 Theoretical interpretation

The two-peak structure in the $3d_{3/2}$ and $3d_{5/2}$ PES spectra of ruthenates have been described in terms of a Mott-Hubbard picture within a DMFT approach by Kim *et al.* [Kim et al., 2004], and cluster calculations of Ru 3d in Sr_2RuO_4 by Okada [Okada, 2002], and recently new cluster calculations by Michel Van Veenendaal [Veenendaal, 2006]. In ruthenates oxides, the energy level of the oxygen 2p orbits is lower than the lower Hubbard band of Ru 4d electrons, thus this system is the Mott-Hubbard system and no charge from oxygen could be transferred to Ru sites and . Although the charge transfer from O 2p orbital to Ru 4d orbital is prohibited under the Mott-Hubbard scheme, the metallic well-screened feature of Ru 3d spectra still can be interpreted by the charge transfer model, where the charge is transferred from the coherent band at E_F to the Ru site rather than from the oxygen bands [Kim et al., 2004]. The coherent band, which are called the quasiparticle states, are occupied by electrons near E_F with a identified momentum and moving under the mean field of the remaining system.

3.3. Results and Discussion

In the Mott-Hubbard type system, such as the ruthenates we studied, the metal to Mott insulator transition can be achieved by changing the ratio of the Coulomb interaction U between conduction electrons to the band width W . When W/U is big (e.g. more than 1), the system exhibits a metallic behavior and then the conduction electrons in the coherent band can move to the Ru $4d$ valence band to screen the core-hole potential. When W/U is very small, the system becomes a Mott insulator and the coherent band is absent due to the insulating gap. Consequently, there is no charge can be transferred from the coherent band and the screened peak in the low binding energy of PES spectra cannot be observed any more, as shown in Fig.3.11. The interpretation of the core-hole screening by quasiparticles is based on the Mott-Hubbard mechanism, where the role of O $2p$ bands is not considered. However, based on the charge-transfer mechanism with a charger transfer from oxygen, the metallic screened peak in Sr_2RuO_4 PES spectra is also produced by the non-local screening effect in $\text{Ru}(d_{xy})_5\text{O}(2p\pi)_{16}$ cluster model performed by Okada [Okada, 2002] and it suggests that the energy separation between well screened peaks and main peaks is reminiscent of Coulomb interaction between Ru $3d$ and $4d$ holes, and is comparable with Ru $4d$ bandwidth. The $4d_{xy}$ orbital occupation has shown an important effect to raise the non-local screening feature as well. More recently, Van Veenendaal performed the multi-Ru-site cluster calculation with consideration of the competition between different orbital degrees of freedom. By introducing an energy difference ΔE between the xy and yz/zx orbitals, changes of Ru $4d_{xy,yz/zx}$ orbital occupation show a drastically effect on the Ru $3d$ XPS spectra [Veenendaal, 2006], as shown in Fig.3.12, where the local screened peak and non-local screened peak are corresponding to the main peak and well screened peak in our Ru $3d$ PES spectra, respectively. Due to the large coupling between the neighboring RuO_6 and the $4d_{xy}$ site in the presence of a core hole, the number of $4d_{xy}$ electrons is important on the weight of non-local screening process and the less xy electrons the stronger non-local screened peak is for the more space to accept a charge transferred into.

However, the existent calculations only provide a general picture for

3.3. Results and Discussion

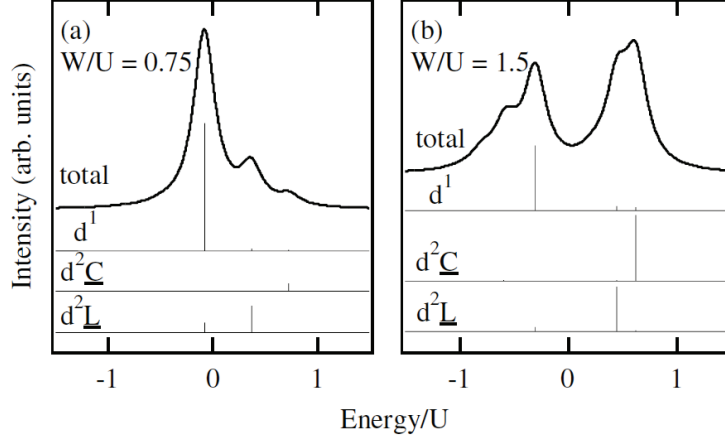


Figure 3.11: Core-level spectra from DMFT calculation with two different W/U by Kim *et al.* [Kim *et al.*, 2004], where $d^1 \equiv d^1 L^2 C^1$ for Ru^{+4} . (a) $W/U=0.75$ is corresponding to the mott insulator and thus the screening from the coherent band $d^2 \underline{C}$ is very weak, where C denotes the coherent peak. (b) $W/U=1.5$ is corresponding to the metal system with a strong screening from the coherent band.

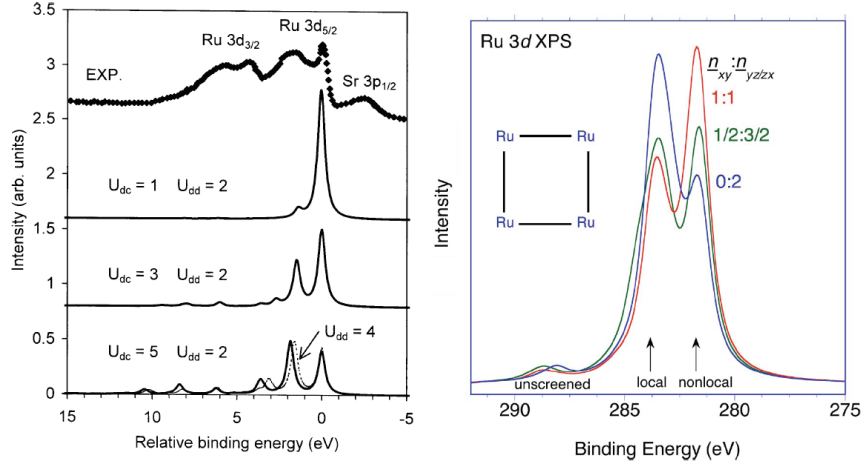


Figure 3.12: Theoretical Ru $3d$ spectra calculated by Okada (Left) [Okada, 2002] and Veenendaal (Right) [Veenendaal, 2006]. Left: $\text{Ru}(d_{xy})_5\text{O}(2p\pi)_{16}$ cluster calculation for $4d_{xy}$ with 1.6 holes. U_{dc} is the coulomb repulsion between $3d$ and $4d$ electrons and U_{dd} is for $4d$ electrons. Right: The orbital occupation effect on the Ru $3d$ spectra. n_{xy} and $n_{yz/zx}$ are the hole numbers in t_{2g} orbitals.

two-peak structure of XPS spectra in Ruthenates. We still cannot conclude what is the screening channel induced a well screened peak in our Ru 3*d* PES spectra, screening by quasiparticles, non-local screening called by Okada, or the mix of those two. Another important question is that how the 3*d* Mn impurities lead to an evolution of screened peak in PES spectra in the 4*d* transition metal and further to answer what is the origin to the MIT, possibly like derived from the charge transfer between t_{2g} orbitals or band width change in Mott-Hubbard mechanism. To obtain the answer for these questions, we may need to consider the competition between local and itinerant states in the system because the strong correlation effects in Mn impurities and weaker electronic correlations in the 4*d* host, and the fact of the hopping behavior of the Mn impurities. Thus the specific theoretical calculation with these considerations is required to perform to quantitatively interpret our experimental results.

3.4 Conclusion

We have studied the Mn impurities dependence of Ru 3*d* spectra in the double-layered ruthenates $\text{Sr}_3\text{Ru}_{(1-x)}\text{Mn}_x)_2\text{O}_7$, both by surface (APE) and bulk (VOLPE) sensitive XPS measurements. The presence of the two-peak structure, the unscreened peak and the screened peak, is confirmed, similar to other ruthenate systems. With increasing the Mn doping level, the well screened peaks become weaker with the becoming more insulating system and this evolution offers a way to investigate the MIT by XPS technique. The surface contribution is determined by fitting the spectra and analysing the ratio of well screened peak to main peak at different photon energies. By comparing with different theoretical calculations, the well screened peak may could be interpreted by the charge transfer between the coherent band and Ru site, and the role of the three t_{2g} orbitals on the screening channel is investigated as well. To further study the MIT in this 4*d* system doped with 3*d* impurities, we perform ARPES investigation to study the low-energy excitation and information of band structures, as shown in the following chapter.

Chapter 4

ARPES Investigation on MIT in Mn-doped $\text{Sr}_3\text{Ru}_2\text{O}_7$

4.1 Introduction

Electronic and lattice instabilities in strongly correlated electron systems give rise to many fascinating phenomena, such as various types of spin, charge, and orbital ordering. This is a common feature in many of the $3d$ transition-metal oxides, with best known examples including the stripe instability in the cuprate superconductors and the magnetic phase separation in manganites. Competing instabilities and ordering phenomena can also be found in the somewhat less correlated $4d$ transition-metal oxides, with the ruthenates being one of the most prominent families. These materials, and in particular the perovskite ruthenium oxides of the Ruddlesden-Popper type $(\text{Sr}/\text{Ca})_{n+1}\text{Ru}_n\text{O}_{3n+1}$, show an extremely wide range of spectacular physical properties, ranging from Mott-Hubbard insulating behavior to spin-triplet multi-band superconductivity, from spin to orbital correlations, and from Fermi liquid to quantum critical behavior [Machenzie et al., 1998]. $\text{Sr}_3\text{Ru}_2\text{O}_7$, which is the subject of this study, is known as a metal on the verge of ferromagnetism [Ikeda et al., 2000]. More recently, magnetic field tuned quantum criticality [Grigera et al., 2001] and electronic nematic fluid behavior [Borzi et al., 2007] have been proposed for this compound and associated with a metamagnetic transition. However, the deeper connection between these effects is still highly debated and its description will depend on a broader understanding of the incipient instabilities in $\text{Sr}_3\text{Ru}_2\text{O}_7$. Magnetic impurities such as Mn have been introduced in $\text{Sr}_3\text{Ru}_2\text{O}_7$ in an attempt

4.1. Introduction

to stabilize the magnetic order in the system. With the inclusion of a few percent of Mn, a MIT was observed in transport experiments, and the emergence of a Mott-like antiferromagnetic state was proposed [Mathieu et al., 2005].

To explore the nature of the MIT induced by Mn impurities, the X-ray absorption spectroscopy (XAS) and resonant elastic soft x-ray scattering (REXS) work on $\text{Sr}_3(\text{Ru}_{1-x}\text{Mn}_x)_2\text{O}_7$ at have been performed by Hossain *et al.* [Hossain et al., 2008, 2009]. Using a combination of XAS and theoretical modeling (cluster and density functional theory calculations), they have discovered that Mn impurities do not exhibit the same 4+ valence in Ru, but rather act as 3+ acceptors. The extra Mn e_g electron occupies the in-plane $3d_{x^2-y^2}$ orbital instead of the expected out of plane $3d_{3z^2-r^2}$. This unusual crystal field level inversion is well described by a physical model they developed, which highlighted the competition between localized 3d states of the impurity and the more delocalized nature of the Ru 4d-O 2p orbitals of the host material. The REXS measurements on Mn edge and Ru edge were performed to investigate the role of Mn impurities in emergence of the insulating phase. REXS measurement detected $q = (\frac{1}{4}, \frac{1}{4}, 0)$ and $(\frac{1}{4}, \frac{3}{4}, 0)$ superlattice peaks appearing below the metal-to-insulator transition temperatures for 5% and 10% Mn systems. These superlattice peaks were proposed to be the result of a zigzag antiferromagnetic ordering formed in the system. It might be surprising that the dilute, randomly distributed Mn impurities induce a long-range ordering pattern. However, considering the correlation between Mn moments and obtaining the correlation lengths from the inverse of the full-width half maximum of the experimental momentum scans, the simulation shows that the superlattice peaks are reproduced based on the long-range spin order pattern with the correlated $S = 2$, 3d-Mn³⁺ impurities, as shown in Fig.4.1. In a summary, REXS results showed that dilute Mn impurities do not only induce long-rang magnetic order but also provide a unique opportunity to probe the electronic instabilities in the parent compound and thereby reveal the mechanism behind the MIT itself. Starting from this point, here we use ARPES to directly probe the ordered phase and the change in the band dispersion with Mn substitution, in order

4.1. Introduction

to further address the mechanism of MIT in $\text{Sr}_3\text{Ru}_2\text{O}_7$ and the role of the low-energy electronic degrees of freedom.

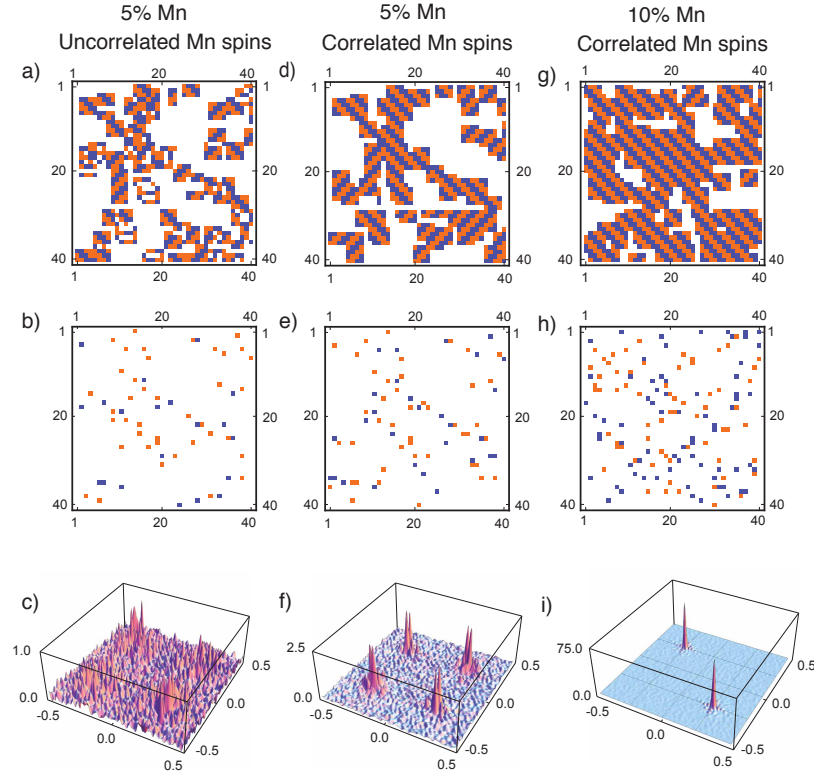


Figure 4.1: (a,d,g) Spin-ordered islands in the RuO_2 plane for various Mn contents and spin correlations: (a) 5% Mn, uncorrelated Mn spins; (d) 5% Mn, correlated Mn spins; (g) 10% Mn, correlated Mn spins. (b,e,h) Corresponding location of Mn impurities with up/down (blue/red) spins. (c,f,i) Reciprocal space map of the Mn scattering intensity generated by averaging over 200 random Mn-impurity distributions, of the kind in (b,e,h), to reduce noise.(from [Hossain et al., 2009])

4.2 Experiment

ARPES experiments over large momentum space region, in pure, 5% and 10% Mn doped $\text{Sr}_3\text{Ru}_2\text{O}_7$ have been carried out on the Electronic Structure Factory endstation at Beamline 7.0.1 as a function of temperature. At high temperature $T = 100$ K, $\text{Sr}_3(\text{Ru}_{1-x}\text{Mn}_x)_2\text{O}_7$ single crystals were cleaved *in situ* at a base pressure better than 2.5×10^{-11} torr and then oriented by taking fast E_F scans. For each doping level sample, FS was acquired at different temperatures, above and below the metal-to-insulator transition temperature. The photon energy scan also was done to show the photon-energy dependence of E_F . The $\text{Sr}_3(\text{Ru}_{1-x}\text{Mn}_x)_2\text{O}_7$ samples we measured are the ultra-clean single crystals most recently grown by our collaborators in the groups led by Y. Yoshida (at AIST in Tsukuba), H. Takagi and Y. Tokura (University of Tokyo). These crystals exhibit superior quality, as evidenced by the low residual resistivity in zero field [Mathieu et al., 2005]. As the ruthenates physics is dramatically sensitive to disorder [Mackenzie and Maeno, 2003], this improvement is key to the success of our experiments.

4.3 Results and Discussion

4.3.1 Fermi surface

In Fig.4.2, we give the first impression of the doping and temperature dependence of FS in $\text{Sr}_3(\text{Ru}_{1-x}\text{Mn}_x)_2\text{O}_7$ (with $x=0, 0.05$ and 0.1) by our ARPES raw data. The photon energy used for these measurements is set at $h\nu=142$ eV, which is the best energy level allow us to observe a finest FS during our beamtime, henceforward all the data shown are taken at $h\nu=142$ eV except a notation is declared. As we see, the shape of raw FSs are slanted and have been rotated by some arbitrary angle, which actually is 14.5° away from y-axis. This angle is chosen as the best oration position to minimize the effect of the polarization of beam and to detect a FS with most features. Looking at the shape of FSs, a strongly doping dependence is clear to see in Fig.4.2, however the change due to the temperature effect is very slight, and only the fermi edge is pushed down as the system becoming an insulator, which we

4.3. Results and Discussion

will prove later. With increasing the Mn concentration, the FS becomes one dimensional (1D), where the two dimensional (2D) feature (such as circles) is almost absent and only 1D straight lines remain on the FS.

After converting the raw data from the angle space into the momentum space and applying a normalization on the intensity of FS, we obtain the FS of $\text{Sr}_3\text{Ru}_2\text{O}_7$ as shown in Fig.4.3(a). Comparing with the FS measured by Tamai *et al.* [Tamai *et al.*, 2008] and the local-density approximation (LDA) calculation for $\text{Sr}_3\text{Ru}_2\text{O}_7$, our FS seems have less features than Tamai's because it is unfolded, but agrees well with the LDA calculation without folding [Singh and Mazin, 2001]. Due to the extreme surface sensitive in ARPES measurement and the widely existed surface (for Sr_2RuO_4) and bulk ($\text{Sr}_3\text{Ru}_2\text{O}_7$) crystal distortions in Ruthenate oxides [Damascelli *et al.*, 2000; Huang *et al.*, 1998], a folded FS is usually expected to be observed as in Fig.4.3(b). The reason why did not observe a such folded FS is still an open question. One of the possible reasons is for the polarized beam we used. On the other hand, the photon energy used in our experiment is $h\nu=142$ eV, which is much higher than the 21.2 eV generated by He-discharge lamp in Tamai's experiment. Furthermore, in order to show the photon energy effect on FS, a photon energy scan is performed at the azimuthal angle equal to zero, as shown in Fig.4.4. At the polar angle equal to 5° , we realize that a new feature named δ could be observed at $h\nu=120$ eV. Indeed, we have observed a contribution from e_g electrons to the FS and more 2D features on FS under $h\nu=120$ eV. The contribution of e_g electrons is labeled by δ in Fig.4.3(b), which is absent from the FS at $h\nu=142$ eV. Although the FS topology relies on the photon energy, the most features of the measured FS with $h\nu=142$ eV is consistent with the LDA calculation, which means our data has a enough reliability to do further analysis. To define the features on the FS, we perform another comparison with the FS of Sr_2RuO_4 [Singh, 1995] as shown in Fig.4.3(d) and the three sheets (usually called α , β and γ) in Sr_2RuO_4 are observed in $\text{Sr}_3\text{Ru}_2\text{O}_7$ as well.

Using the same names for these three sheets in FS of Sr_2RuO_7 , as illustrate in Fig.4.3(a, c), the α sheet is the square cylindrical hole pocket around X, deriving from the odd combinations of d_{xz} and d_{yx} orbitals; the

4.3. Results and Discussion

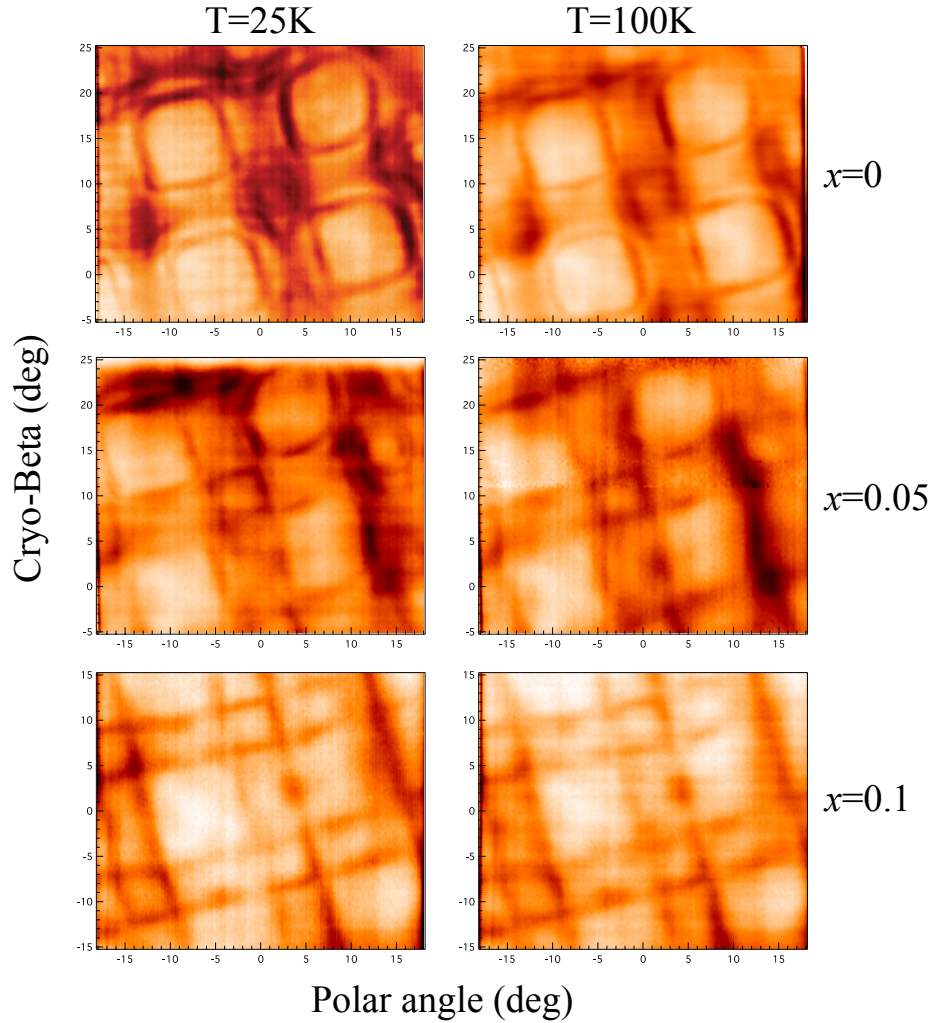


Figure 4.2: Raw FS for $\text{Sr}_3(\text{Ru}_{1-x}\text{Mn}_x)_2\text{O}_7$ with $x=0, 0.05$ and 0.1 from ARPES measurements with $h\nu=142$ eV. The 5% and 10% Mn doped samples have a metal to insulator transition as temperature cooled from 100 K to 25 K, referred to the resistant measurement in Fig.3.1.

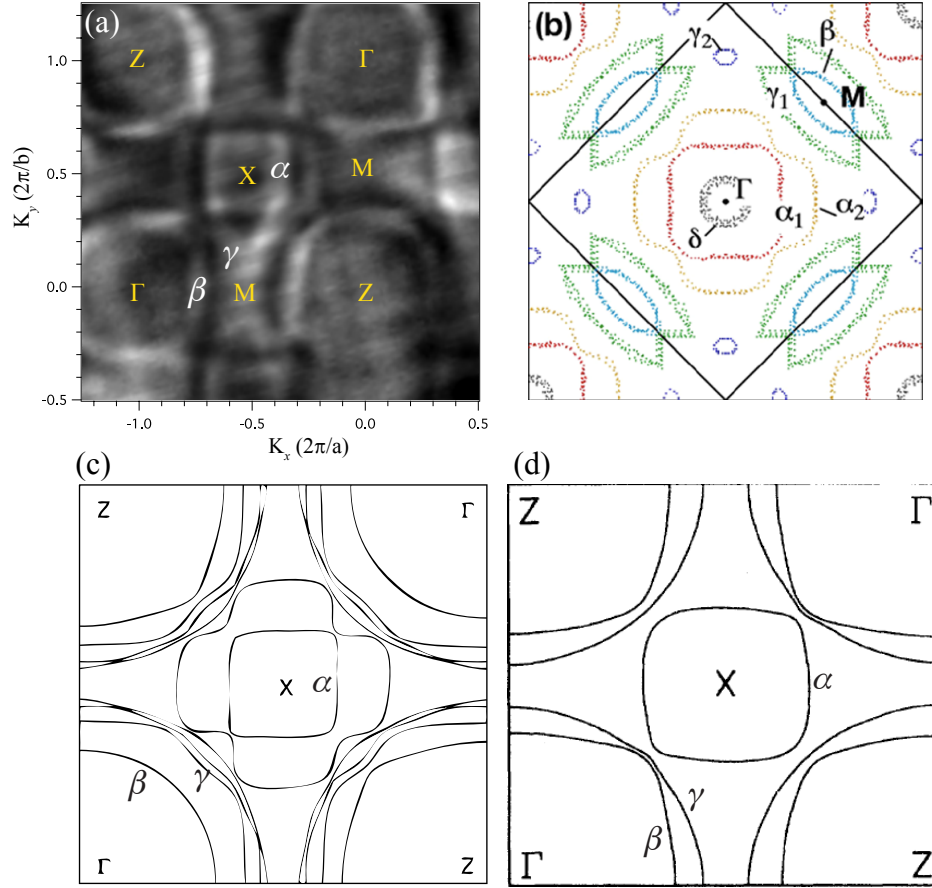


Figure 4.3: (a) FS of $\text{Sr}_3\text{Ru}_2\text{O}_7$ measured at beam line BL 7.0 of ALS with $h\nu = 142$ eV at $T = 25$ K. The intensity of FS is normalized along both k_x and k_y directions. (b) FS contours of $\text{Sr}_3\text{Ru}_2\text{O}_7$ measured at beam line V-4 of SSRL with $h\nu = 21.2$ eV at $T = 9$ K by Tamai *et al.* [Tamai *et al.*, 2008]. Note the FS is folded. (c) Basal plane FS of $\text{Sr}_3\text{Ru}_2\text{O}_7$ in the ideal tetragonal structure from LDA calculation [Singh and Mazin, 2001]. Note this FS is unfolded. (d) FS of Sr_2RuO_7 in the basal plane of the body-centered-tetragonal zone [Singh, 1995].

4.3. Results and Discussion

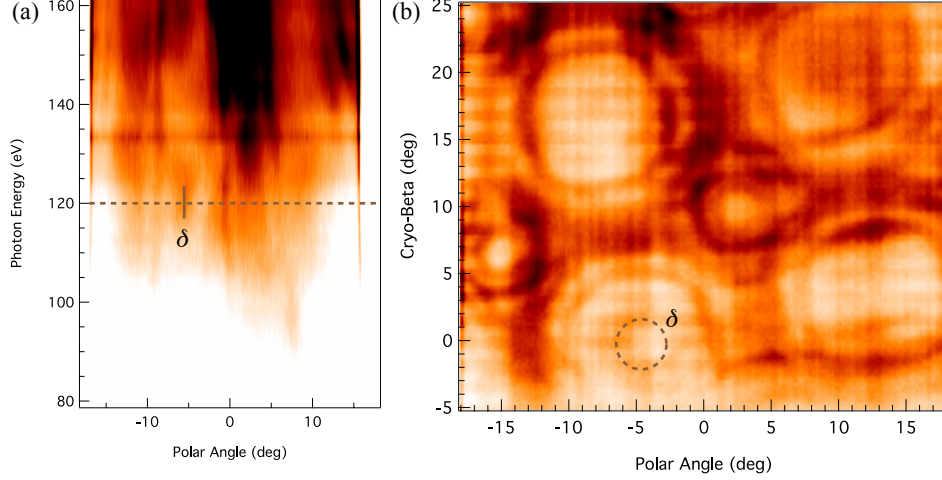


Figure 4.4: (a) Photon energy scan performed with $h\nu=80$ eV to 160 eV in $\text{Sr}_3\text{Ru}_2\text{O}_7$ at 25 K. (b) Raw FS of $\text{Sr}_3\text{Ru}_2\text{O}_7$ measured at 25 K with $h\nu=120$ eV. The dashed circle is drawn for the appearance of e_g electrons from $d_{x^2-y^2}$ orbital on FS.

β sheet is the innermost cylinder electronic pocket around Γ and it is also mainly d_{xz}/d_{yz} orbitals derived; the γ sheet is referring to the outside circular cylinder around Γ , which is actually a bunch of three cylinders around Γ in LDA FS and we however cannot distinguish them in the experimental FS, due to a limit of the momentum resolution. The γ sheet is also an electronic pocket and is mainly derived from the d_{xy} orbital, but is mixed with d_{xz}/d_{yz} character in $\text{Sr}_3\text{Ru}_2\text{O}_7$ FS. Beside these three sheets, there is an additional sheet on the FS of $\text{Sr}_3\text{Ru}_2\text{O}_7$, which is the cross-shape hole pocket around X and LDA calculation proposes that it is derived from the odd combinations of d_{xz} and d_{yz} orbitals. Since the FS we show is only in the $k_x - k_y$ plane, the electrons from d_{xz} (d_{yz}) orbital only can form a 1-D band along k_x (k_y) direction in $k_x - k_y$ plane and result in a FS with straight lines, such as α , β sheets. The electrons of d_{xy} orbital however have no restriction to move around in the plane and would induce a circular γ sheet as a result of 2-D band.

4.3.2 Enhanced FS nesting with Mn doping

The shape of FS often conveys rich information on a variety of ordering phenomena in physics systems. A nesting vector q in the FS determines the periodicity of the modulation of the conduction electrons, and such spin- and charge-density waves [Fawcett, 1988] are two examples of the FS driven ordering. In the REXS measurement, the role of Mn impurities was suggested to primarily stabilize the ordering incipient in the parent compound and it introduced a zigzag spin-ordering pattern in the insulating region [Hossain et al., 2009]. Thus we could expect to observe a stronger and possible modified nesting vector in the FS of Mn-doped $\text{Sr}_3\text{Ru}_2\text{O}_7$ at low temperature, due to the spin ordering, in comparison with the pure $\text{Sr}_3\text{Ru}_2\text{O}_7$ and other ruthenium oxides already studied by us and other groups [Damascelli et al., 2000, 2001; Shen et al., 2001; Ingle et al., 2005; Baumberger et al., 2006; Tamai et al., 2008]. Indeed, in Fig.4.2 we have already seen that the Mn impurities strongly enhance the FS nesting, and lead to the emergence of a 1-D featured FS. To quantitatively analyze the change of the nesting vector due to the Mn impurities, we carefully measure the length of the nesting vector in the momentum space for different doping levels. In Fig.4.5, the 1D feature of β sheet is highlighted by the red-line frame. The nesting vector derived from β sheet in the pure sample is given by the red arrows. Setting the Γ point as an origin, the positions of corners of two β sheets in the diagonal way are $(-0.3, 0.3)$ and $(-0.72, 0.71)$, with the units of $2\pi/a$ and $2\pi/b$ for k_x and k_y respectively, where the lattice constants a and b in the xy plane are little different (less than 0.1 \AA) based on the determination of period in our FS mapping, although they are usually the same in crystal. Henceforward, the units of nesting vectors are set to $2\pi/a$ by assuming $a \equiv b$ for simplicity. The possible nesting vector due to the straight part of β sheets is $q_\beta=(0.42, 0, 0)$ or $(0, 0.41, 0)$, which is the gap between the nearest two β sheets. Another nesting vector due to the α sheet is smaller and is equal to $q_\alpha=(0.29, 0, 0)$ or $(0, 0.28, 0)$, as shown in Fig.4.3(a). Because both the 1D feature of β and α sheets, there is a possible good nesting vector originated from these two sheets, which is along the ΓX way and equals to the

4.3. Results and Discussion

distance between the top or bottom corners of β and α sheets. The length of this nesting vector $q_{\alpha\beta}$ should be between q_β and q_α , which is measured as $q_{\alpha\beta} = (0.36, 0.36, 0)$. In Sr_2RuO_4 , the nested topology due to α and β FS with $q_{\alpha\beta} \approx (\pm 0.33, \pm 0.33, 0)$ is confirmed both in ARPES [Damascelli et al., 2000] and inelastic neutron scattering experiments, which is approximately equal to the $q_{\alpha\beta}$ in $\text{Sr}_3\text{Ru}_2\text{O}_7$ and exactly equal to the $q_{\alpha\beta}$ in 10% Mn doped sample as shown by following.

In Fig.4.6, the two FS of $\text{Sr}_3(\text{Ru}_{0.95}\text{Mn}_{0.05})_2\text{O}_7$ taken at different beam time (2005 and 2009, respectively) in ALS are shown. Both of these two data set demonstrate that by introducing Mn impurities the distortion of FS starts to appear, in particular fade away the γ FS. However, the features of α and β sheets, shape and size, still roughly remain the same, as illustrated using dark-line frame for β , dash line for α and their corner positions in Fig.4.6(a). In Fig.4.6(b), the cross-shape hole pocket around X point is still observable as well. Thus we would like to claim that the Mn impurities have a strong effect to destroy the γ sheet and make the 1D bands become dominate on FS. Another change we should point out is that the α and β sheets seem to get touch with each other in the 2005 year's data. However, both in $\text{Sr}_3\text{Ru}_2\text{O}_7$ and Sr_2RuO_4 , they are split apart and a LDA calculation has demonstrated it as a effect of the spin-orbital coupling [Haverkort et al., 2008]. The corresponding nesting vector $q_{\alpha\beta} = (0.36, 0.36, 0)$ is the same as in the undoped sample. To understand these changes on the FS, we have to check the FS nesting and shape in the higher Mn doped system.

When the doping level of Mn impurities is increased to 10%, the FS becomes 1D FS composed of straight lines and the two dimensional γ sheet from d_{xy} band is missing, as seen in Fig.4.7. The straight lines are parallel or perpendicular to each other, and form a fantastic remarkable nesting vector, which is $q_{\alpha\beta} = (0.33, 0.33, 0)$ as the same as the nesting vector in Sr_2RuO_4 . Comparing with $q_{\alpha\beta}$ in the undoped sample, we learn that the Mn impurities have an attempt to reduce the length of $q_{\alpha\beta}$. The reduced $q_{\alpha\beta} = (0.33, 0.33, 0)$ means that an ordering with a modulation period of 3 lattice constants is introduced into the system. However, in REXS measurement the superlattice peak is at $q = (0.25, 0.25, 0)$, which is smaller than the

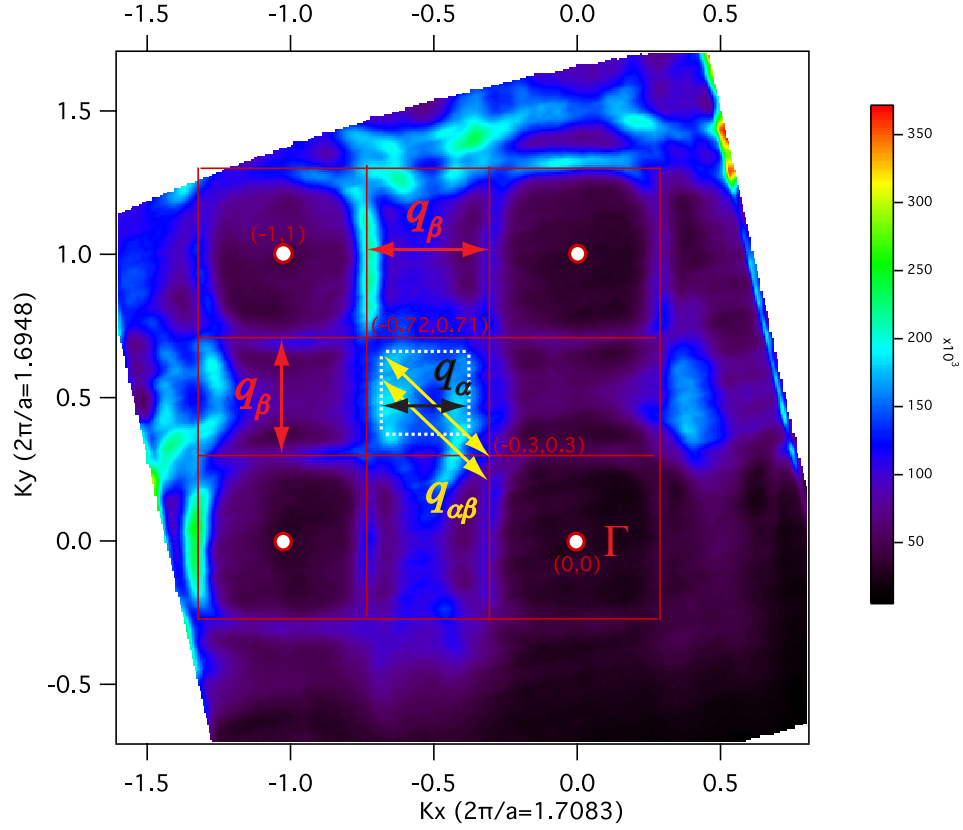


Figure 4.5: Nesting vector check in FS of $\text{Sr}_3\text{Ru}_2\text{O}_7$. The red-line frame is to highlight the 1D feature of β sheet, and the white-line square is to highlight the α sheet, which is clearly shown in the normalized FS in Fig.4.3(a). The possible nesting vectors derived from β and α sheets are: $q_\beta=(0.42, 0, 0)$ or $(0, 0.41, 0)$, $q_\alpha=(0.29, 0, 0)$ or $(0, 0.28, 0)$, and $q_{\alpha\beta}=(0.36, 0.36, 0)$ with $2\pi/a$ as units.

4.3. Results and Discussion

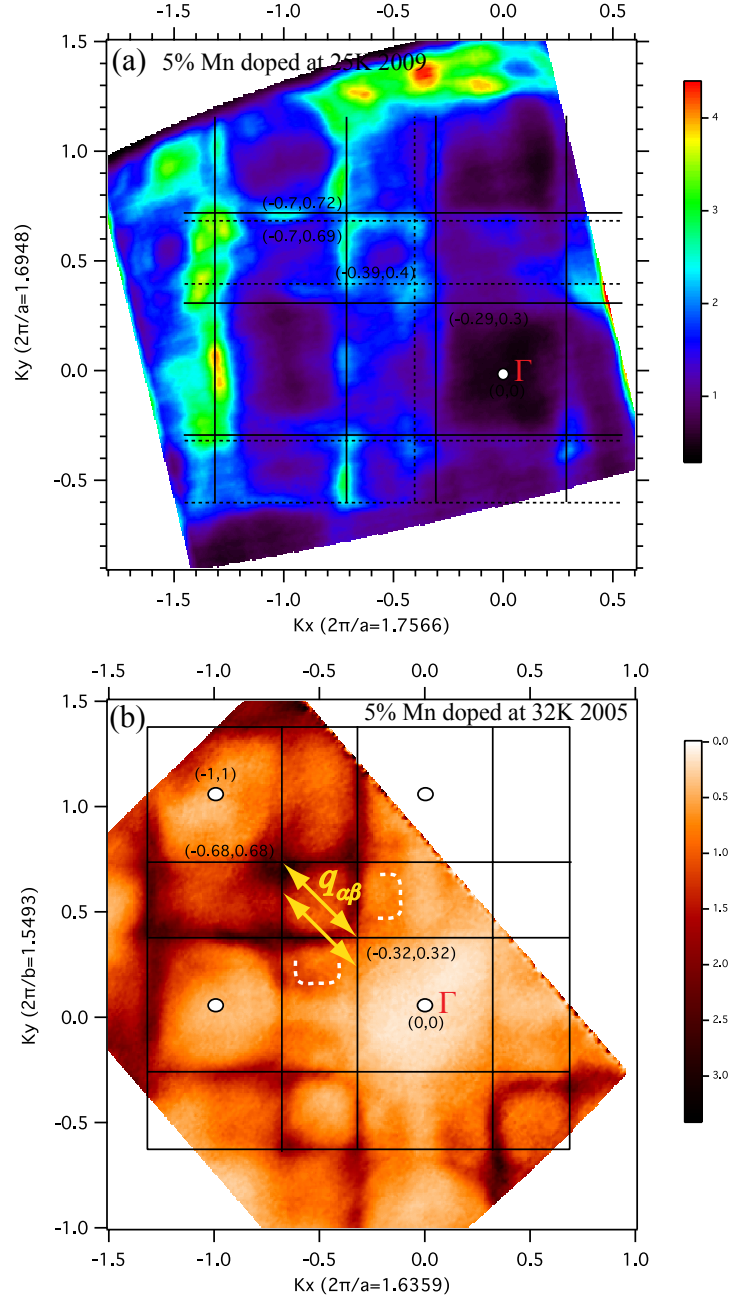


Figure 4.6: FS of $\text{Sr}_3(\text{Ru}_{0.95}\text{Mn}_{0.05})_2\text{O}_7$. (a) The data are taken with $h\nu=142\text{eV}$ at $T = 25\text{ K}$ in ALS in 2009. (b) The data are taken with $h\nu=82\text{eV}$ at $T = 32\text{ K}$ in ALS in 2005. The cross-shape hole pocket is visible as shown by two white dashed lines.

4.3. Results and Discussion

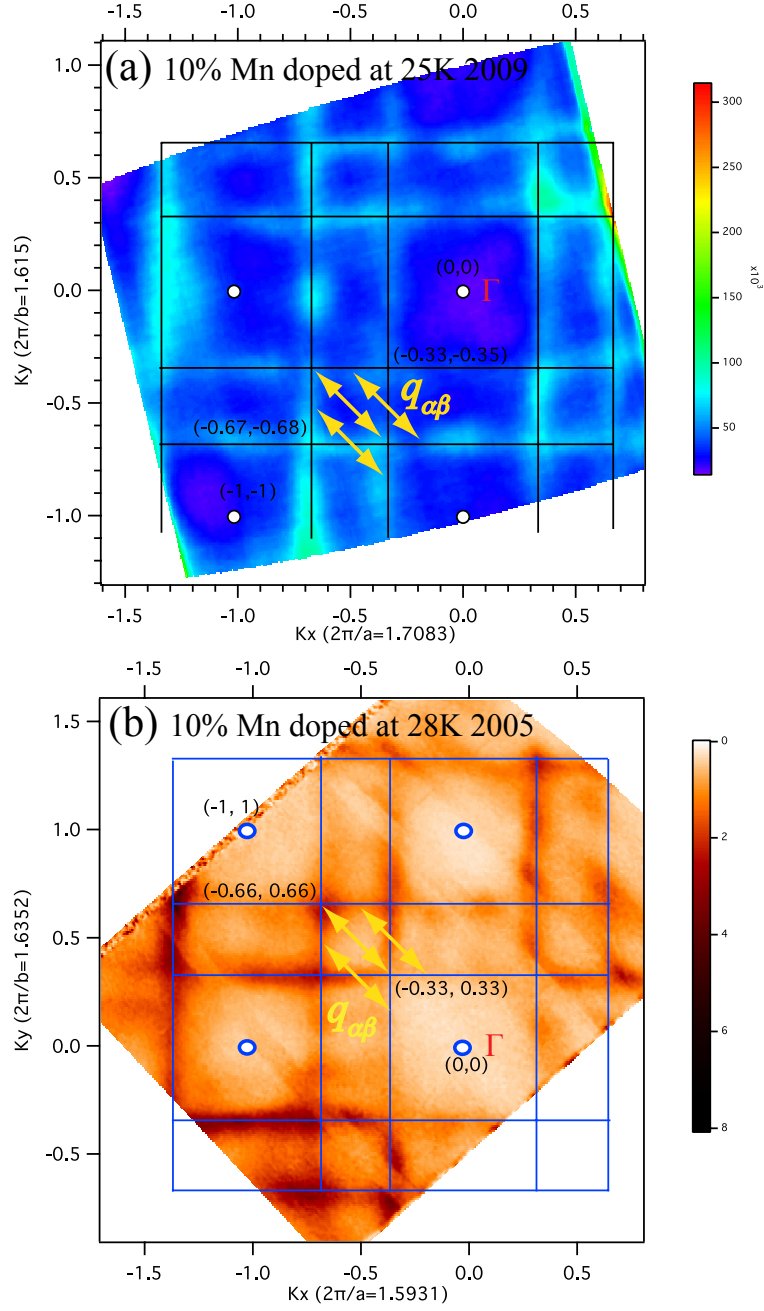


Figure 4.7: FS of Sr₃(Ru_{0.9}Mn_{0.1})₂O₇. (a) The data are taken with $h\nu=142\text{eV}$ at $T = 25\text{ K}$ in ALS in 2009. (b) The data are taken with $h\nu=82\text{eV}$ at $T = 28\text{ K}$ in ALS in 2005. Both of them have a nesting vector $q_{\alpha\beta}=(0.33, 0.33, 0)2\pi/a$.

4.3. Results and Discussion

nesting vector from FS and is corresponding to the four times expanded BZ with up-up-down-down spin configuration. A possible explanation on the difference of q between ARPES and REXS is given at the end of this chapter by considering the difference between charge- and spin-ordering. Here, an important issue we have to emphasize is that both the area of α and β sheets are expanded, and then these two sheets join to form a 1D FS. As we mentioned in the previous paragraph, the spin-orbital coupling is the cause proposed to explain the no mixing among α , β and γ sheets in Sr_2RuO_4 [Haverkort et al., 2008]. Now the mixing of α and β by doping Mn impurities may suggest us to perceive a fact that the spin-orbital coupling effect is suppressed by Mn doping as the system becoming an insulator.

According to Luttinger's theorem, the FS volume is an important parameter to describe the electron (hole) occupation of an orbital by analyzing the size of electron pockets (hole pockets) on FS. For example, the increased volume of α FS means the decreased occupation of electrons of the corresponding $d_{yz/xz}$ bands, because α sheet is the hole pocket. Since the ARPES measurement only provides a 2D FS, the FS area can be directly measured rather than the volume. However due to the very weak dispersion of FS along k_z in ruthenates system [Bergermann et al., 2000; Bergemann et al., 2003], the FS volume is approximately proportional to the FS area. A summary of the closed FS volume of α and β FS with/without Mn doping is shown in Table 4.1. Comparing to the FS volume in Sr_2RuO_4 determined by dHvA measurements [Machenzie et al., 1998], where the FS volume of α and β are 10.8% and 45.7% of BZ volume, respectively, we can see the same FS volume both in the single-layered (Sr_2RuO_4) and double-layered ruthenates ($\text{Sr}_3\text{Ru}_2\text{O}_7$). In Table 4.1, from undoped case to 10% Mn doped

Table 4.1: FS volume of α and β sheets with/without Mn doping.

FS volume (% BZ) at 25 K	α (h^+ , xz, yz)	β (e^- , xz, yz)
Undoped	9.0	34.1
10%Mn doped	11.2	45.1

case, the closed hole pocket α sheet has a 2.2% volume of BZ increased, and thus the electron occupied volume of α sheet is decreased by 2.2%; the β sheet (the electron pocket) has a 11% BZ volume increased. Thus, the total electron occupation of the α and β sheets is increased by 8.8%, which means that some additional charges have been transferred into the related $d_{xz/yz}$ bands by Mn doping. The source to provide these additional charges is still ambiguous if only by analyzing the FS, because the missing γ sheet in the 10% Mn doped FS is a puzzle until now and the doping dependence of the cross-shape hole pocket on FS is not easy to be resolved.

4.3.3 Energy and momentum distribution curves

To address the puzzle of the missing γ sheet, in the other word the d_{xy} band on the FS, we use the energy distribution curves (EDC) and momentum distribution curve (MDC) to check the dispersion of the low-energy band structure with changing the Mn doping, as shown in Fig.4.8 - 4.13. EDC is the plot of intensity versus binding energy at a fixed emission angle (or k point); MDC is the plot of intensity versus emission angle (or \mathbf{k}) at a fixed binding energy). If we cut the FS along the high-symmetry direction Γ -M- Γ , we will cross two β and two γ edges around M point. At a glance at the MDCs along Γ -M- Γ for undoped, 5% and 10% Mn doped samples (Fig.4.8, Fig.4.10 and Fig.4.12), two peaks assigned to two β sheets are clearly seen in all three samples and the evolutions of β peaks with binding energy for different doping levels are very similar as slightly separating away as going to higher binding energy, e.g. from E_F to $E_B = -200\text{meV}$, the distance between β peaks d_{peaks} is expanded from 0.41 to 0.47 for undoped, from 0.36 to 0.41 for 5% Mn doped and from 0.33 to 0.37 for 10% Mn doped, with the units of $2\pi/a$. However a dramatic change of peaks assigned to γ sheets is observed by Mn doping. In the undoped $\text{Sr}_3\text{Ru}_2\text{O}_7$ (Fig.4.8), at E_F , the two γ peaks are very close and it means two γ sheets on the FS almost touch each other at the M point. As going to the deeper energy level, these two γ peaks start to separate away quickly comparing to the behavior of β peaks, and then each γ peak is getting closer to its neighboring β peaks. When

4.3. Results and Discussion

$\text{Sr}_3\text{Ru}_2\text{O}_7$ is dilutely doped by 5% Mn (Fig.4.10), a strong noise on MDCs is observable, but we still can recognize the β and γ peaks. Comparing with the undoped case, the d_{peaks} for two γ peaks is not very sensitive to E_B any more, rather keeps a proximate constant as function of E_B . Remember that at E_F two γ peaks are very close to each other in undoped case, but they are well separated in 5% Mn doped sample. This change can be considered as a result by lowering the E_F or consequently lifting d_{xy} band related to the E_F , which possibly causes the fade of γ sheet on FS with Mn doping. The evidence of the down shift of E_F is clear seen by comparing the EDCs from the with and without Mn doping samples. As shown in Fig.4.9, Fig.4.11 and Fig.4.13, the fermi edge of each curve in EDCs is very sharp for a metallic system (undoped), but is getting broad and moves down to the low binding energy as the system becomes an insulator with Mn doping. If the change of γ FS is truly due to the lift of d_{xy} band, we would expect to observe a stronger evidence from the 10% Mn doped measurement. By looking at the EDCs of 10% Mn doped sample, the E_F indeed has been much shifted down, in comparison with the undoped and 5% Mn doped cases. However, since the γ peaks are already absent in MDCs at 10% Mn doping level, we cannot tell the evolution of d_{xy} band from 5% to 10% Mn doping level. In Fig.4.12, the noise on MDC is suppressed as comparing to that of 5% Mn doped and only two mains peaks are observable for us which are assigned to β . The absent of γ peaks could have two possible explanations: first, the d_{xy} band is totally unoccupied now because it is lifted above the E_F or by some other unkown reasons, and then results in the disappearance of γ peaks; second, the γ peaks actually remain on the MDCs, but they are extremely close to the β peaks and become undistinguishable from the β peaks. The reason that we propose the second explanation is based on a combination of two phenomenon: the quick separation of γ peaks as function of E_B in undoped case and the likely lift of d_{xy} band in 5% Mn doped case. On the other hand, the β peak in 10% Mn doped case is broad and a weak split of each peak is visible, which is possible due to the γ and β peaks, although this split is also likely a result of the noise.

The impurity-induced disappearance of d_{xy} band on the FS has been

4.3. Results and Discussion

observed in the insulator region of the ruthenate oxide $\text{Ca}_{2-x}\text{Sr}_x\text{RuO}_4$ [Wang et al., 2004; Neupane et al., 2009], which is the prototype of an orbital selective Mott transition (OSMT) proposed by Anisimov *et al.* to describe the coexistence of itinerant electrons and localized moments in transition metals (TM) with nearly degenerated d -orbitals [Anisimov et al., 2002]. In the $\text{Ca}_{2-x}\text{Sr}_x\text{RuO}_4$ with $x=0.2$ case, the absence of d_{xy} band from FS is caused by the fully filled d_{xy} band. The d_{xy} band is fully occupied by accepting electrons transferred from the 1D $d_{xz/yz}$ bands, because the Ca content increases the rotation and tilting of the RuO_6 octahedra, and the consequent crystal field lowers the energy level of d_{xy} band to below the E_F . Another example that has a missing xy -band FS is Sr_2RhO_4 [Kim et al., 2006; Liu et al., 2008], where Rh has one more $4d$ electron than Ru. This one more electron would increase the volume of electronlike pocket β and γ sheets, however the FS obtained by ARPES measurement did not observe the γ sheet. Through the density-functional electronic structure calculation, it shows that the vanishing of the γ sheet is due to the fully filled d_{xy} band, because the rotation of octahedra results in the hybridization of e_g and t_{2g} states and the gap opened by hybridization consequently pushes d_{xy} band below E_F . In summary, in these two cases, $\text{Ca}_{1.8}\text{Sr}_{0.2}\text{RuO}_4$ and Sr_2RhO_4 , the principle for the missing γ FS is the same and both due to the fully filled d_{xy} band resulted by the rotation of octahedra. In our $\text{Sr}_3(\text{Ru}_{1-x}\text{Mn}_x)_2\text{O}_7$ system, however, the principle for the missing d_{xy} FS may be in contrast to the above two cases, because the d_{xy} band is observed being possibly lifted in our data and the missing d_{xy} FS may be due to the empty d_{xy} band rather than the fully occupied d_{xy} band.

4.3. Results and Discussion

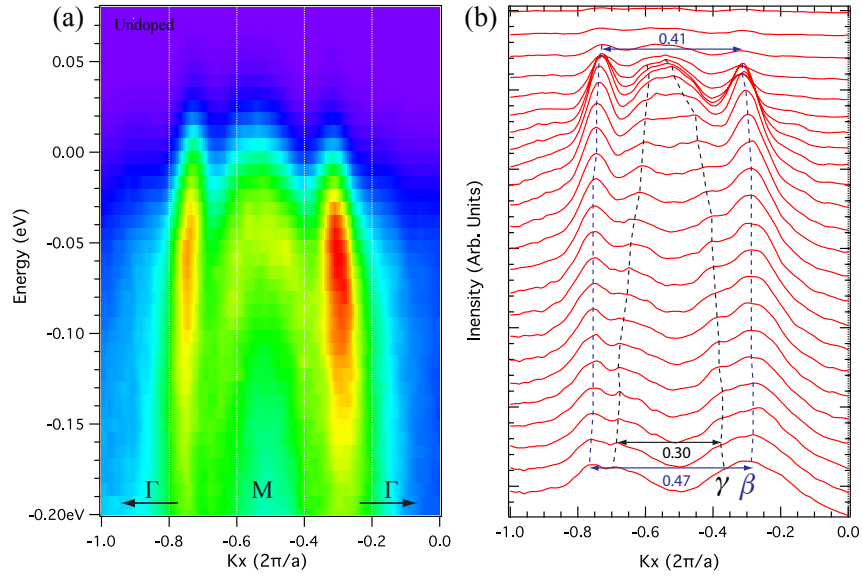


Figure 4.8: (a) ARPES intensity plot along Γ -M- Γ in $\text{Sr}_3\text{Ru}_2\text{O}_7$ at $T = 25$ K. (b) Corresponding MDCs show the low-energy band dispersion for $d_{xz/yz}$ (β) and d_{xy} (γ) bands, indicated by blue lines and dark lines, respectively.

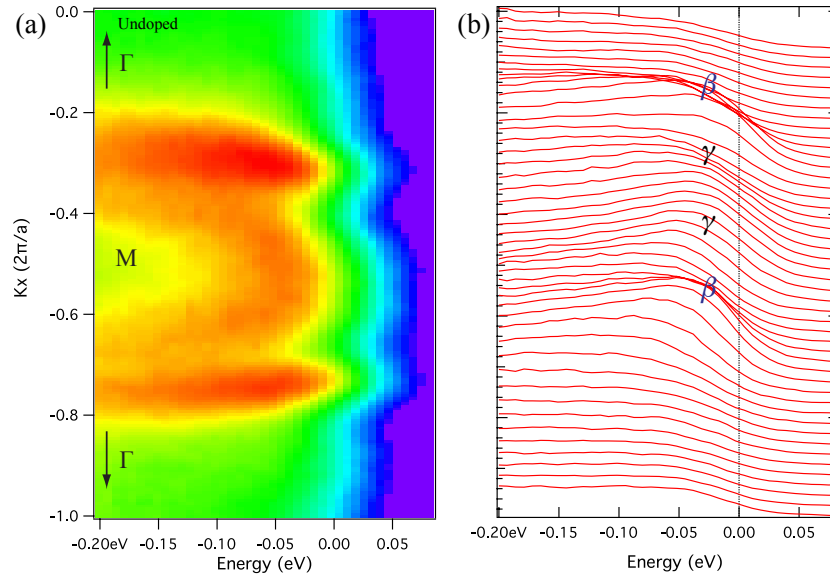


Figure 4.9: (a) ARPES intensity plot and (b) EDCs, along Γ -M- Γ in $\text{Sr}_3\text{Ru}_2\text{O}_7$ at $T = 25$ K.

4.3. Results and Discussion

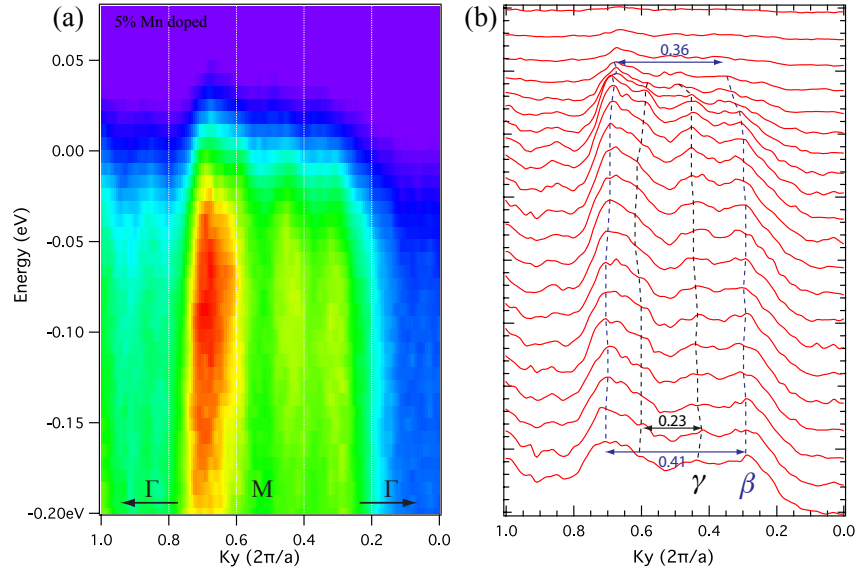


Figure 4.10: (a) ARPES intensity plot and (b) MDCs, along Γ -M- Γ in $\text{Sr}_3(\text{Ru}_{0.95}\text{Mn}_{0.05})_2\text{O}_7$ at $T = 25$ K.

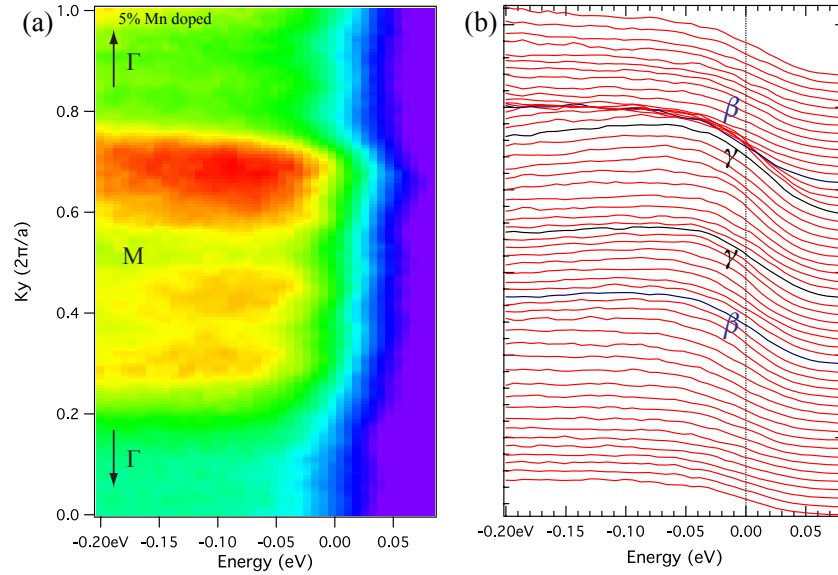


Figure 4.11: (a) ARPES intensity plot and (b) EDCs, along Γ -M- Γ in $\text{Sr}_3(\text{Ru}_{0.95}\text{Mn}_{0.05})_2\text{O}_7$ at $T = 25$ K.

4.3. Results and Discussion

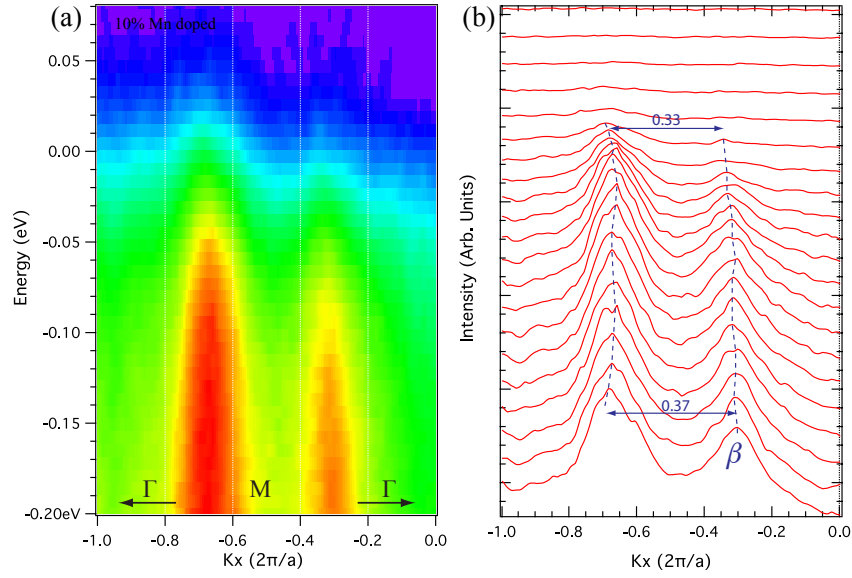


Figure 4.12: (a) ARPES intensity plot and (b) MDCs, along Γ -M- Γ in $\text{Sr}_3(\text{Ru}_{0.9}\text{Mn}_{0.1})_2\text{O}_7$ at $T = 25$ K.

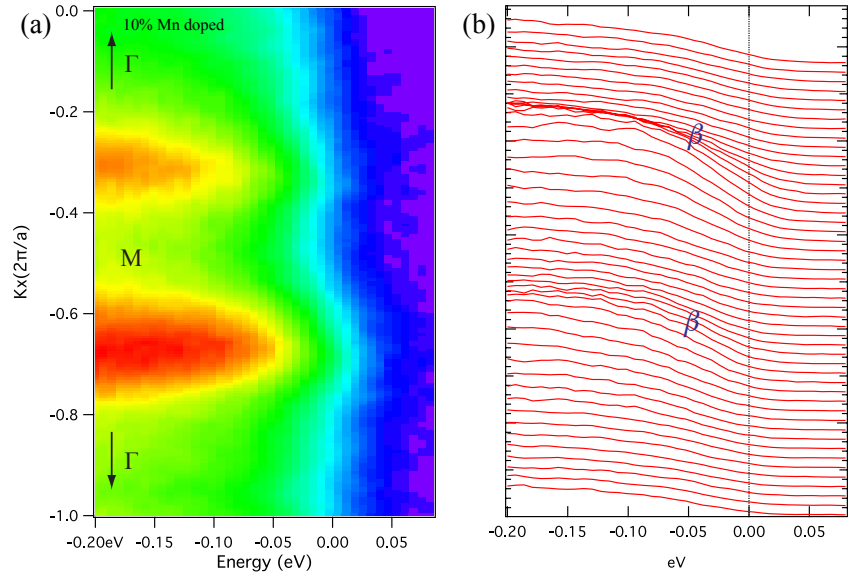


Figure 4.13: (a) ARPES intensity plot and (b) EDCs, along Γ -M- Γ in $\text{Sr}_3(\text{Ru}_{0.9}\text{Mn}_{0.1})_2\text{O}_7$ at $T = 25$ K.

4.3.4 Energy gap opening

When a system is doped by impurities and experiences a metal-insulation transition, usually there is an energy-gap open on the bands crossing E_F . This gap results in no more bands crossing E_F , which is a band-structure picture for an insulator. As we have discussed in the last section, the chemical potential is very important for the study of the change of γ sheet with Mn doping. Here we would like to quantitatively describe the opening of an energy gap in terms of doping level and temperature. In Fig.4.14, we see that the position of fermi edge moves according with the insulating level of a system, namely the higher binding energy of the fermi edge the better insulator it is, which means a gap is opened in the insulating system. For example, $\text{Sr}_3\text{Ru}_2\text{O}_7$ at 25 K is the best metallic system and the 10% Mn doped sample at 25 K is the best insulator in our measurements. The shift of fermi edges is 50meV, which is the result of opening an energy gap and causes the MIT to happen. Comparing to the prototype Mott-Hubbard system V_2O_3 [Mo et al., 2003; Held et al., 2001; Poteryaev et al., 2007], the spectral shape of our EDC is similar to that in V_2O_3 with the presence of the quasiparticle peak [Rodolakis et al., 2009]. Thus, we also can decompose the EDCs by two components: the Hubbard band and the quasiparticle peak. For example, the 10% Mn doped EDC has the Hubbard band at about -1.0 eV binding energy and a quasiparticle peak at about -0.24 eV. The loss of the quasiparticle peak's spectra weight can be observed as system going from metal to insulator. In the undoped sample at 25 K, this metallic system has a vivid sharp quasiparticle peak as shown by the blue line in Fig.4.14. Undergoing a MIT, the intensity of the quasiparticle peak is dramatically suppressed and the spectra become broad in the insulating system (i.e. 10% Mn doped sample at 25 K), accompanied by opening an energy gap. More over, we should note that all the trends for fermi edge and quasiparticle peaks with Mn doping are the same for different k points on the FS. Therefore, we arrive a conclusion that the MIT induced by Mn doping is achieved by suppressing the quasiparticle states and opening an energy gap.

4.3. Results and Discussion

Until now because of the significant change of FS with Mn doping, we paid most of the attention on the Mn doping induced MIT at low temperature. However, at a fixed doping level, such as 10% Mn doped case, the variety of temperature can lead to the onset of a MIT as well. At the room temperature, the 10% Mn doped system is metallic and presents an insulating behaviors at a temperature below $T_c \approx 55$ K. In Fig.4.15, we show the dependence of the position of fermi edges through the EDCs at $\mathbf{k}=(-0.68, 0.68)2\pi/a$, where is the touch point of α and β sheets on the FS. The fermi edge is shifted to the higher binding energy by 35 meV when the sample is cooled down from $T=106$ K to 25 K, but the shape of the spectra remains the same and it indicates temperature independence of the quasiparticle states in the spectra. Thus, the effect of temperature might be to push some bands down to the higher binding energy and result in opening an energy gap. To convert the total number of electrons in the system, pushing down bands has to be accompanied by lifting other bands or by the appearance of some superstructure, such as the spin-ordered magnetic superstructure, which are also the possible results of the temperature effect in the system. To clarify, we have to mention that only the data at $T = 106$ K and 25 K is measured at the stable temperature condition, others are measured during a fast cooling down procedure. Thus we cannot trust the relative big change of chemical potential from $T = 106$ K to 100 K as well as that from $T = 28$ K to 25 K. Nevertheless, the 35meV shift of chemical potential from $T = 106$ to 25 K is reliable. Since the pattern of FS is almost the same for above and below T_c , and only the intensity distribution is varied due to the shift of the fermi edge, as shown in Fig:4.16, the temperature induced MIT is accompanied with only the opening of an energy gap.

4.3. Results and Discussion

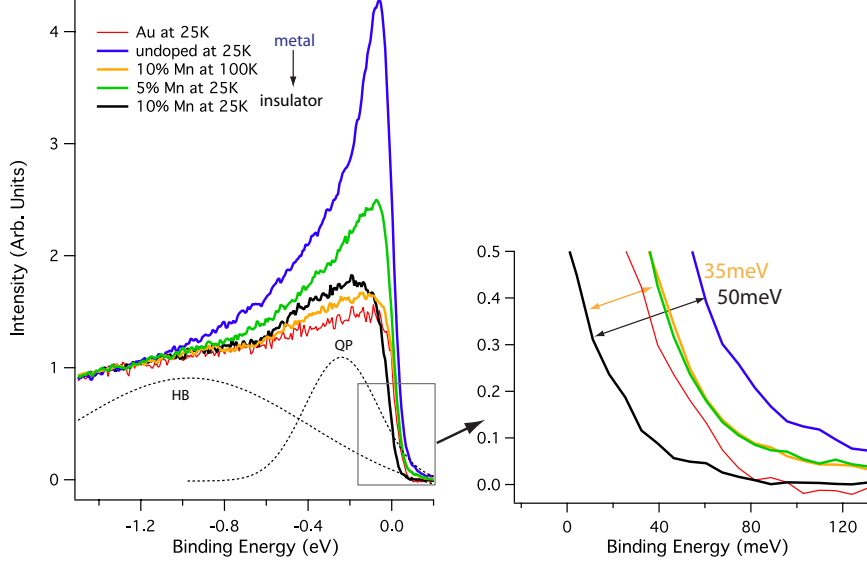


Figure 4.14: EDCs at $\mathbf{k}=(-0.68, 0.33)2\pi/a$ are normalized by the height at $E_B=-1.5$ eV. The back-dashed lines are the two-peak Gaussian fitting for 10% Mn at 25 K, which present the Hubbard band (HB) and the quasiparticle peak (QP), respectively. From metal to insulator, the opening of an energy gap is indicated by the 50 meV shift of fermi edge. For 10% Mn doping, and the quasiparticle peak is heavily suppressed as well.

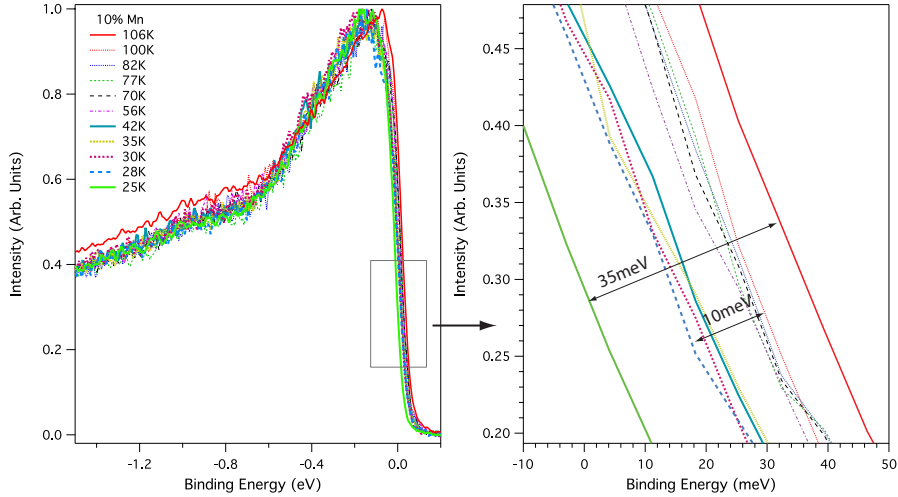


Figure 4.15: In $\text{Sr}_3(\text{Ru}_{0.9}\text{Mn}_{0.1})_2\text{O}_7$, the temperature dependence of the fermi edge indicates the MIT occurred around $T_c=50$ K.

4.3. Results and Discussion

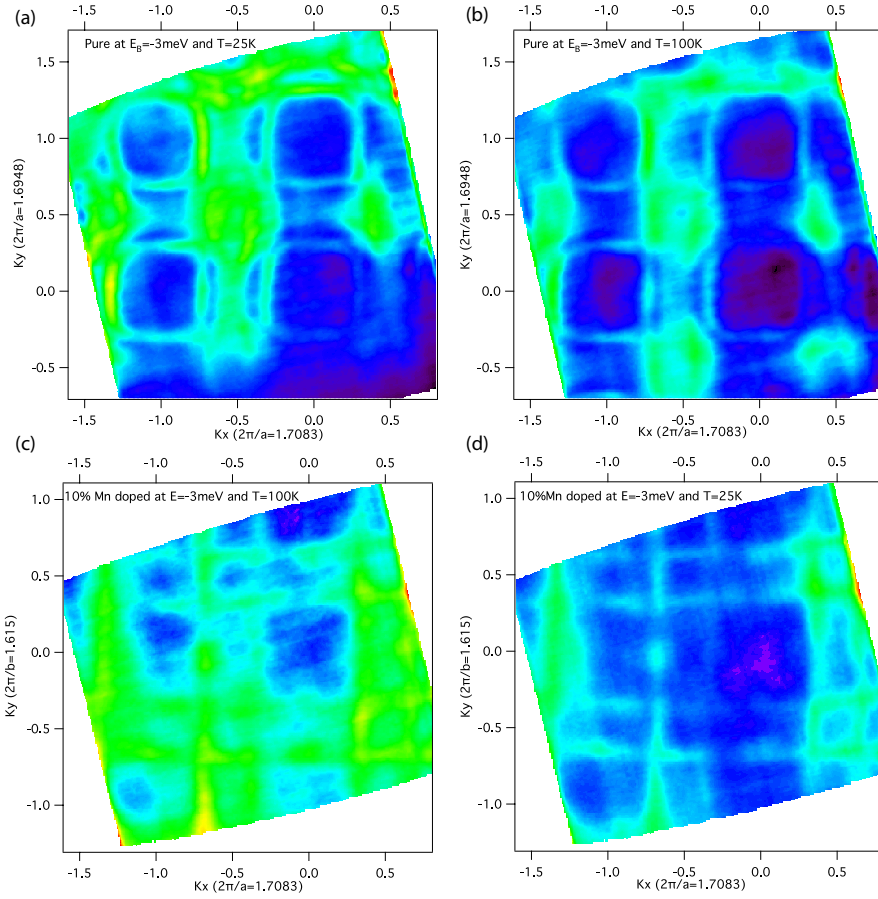


Figure 4.16: Temperature effect on the FS in the undoped (a,b) and 10% Mn doped (c, d) sample. The FSs are obtained by integrating the energy over a ± 3.5 meV window at $E_B = -3$ meV. The FS with more intensity is corresponding to the more metallic systems, which are (a) the undoped sample at 25K and (c) the 10% Mn doped sample at 100 K.

4.3.5 Band structure calculation

The important role of the spin-orbit coupling (SOC) in ruthenates has been demonstrated both for insulating and metallic ruthenates in previous works [Mizokawa et al., 2001; Haverkort et al., 2008]. In the insulating ruthenates $\text{Ca}_{2-x}\text{Sr}_x\text{RuO}_4$, SOC is thought to be strongly correlated with the structure distortion, the rotation and tilt of the RuO_6 octahedron [Oguchi, 2009]. In Sr_2RuO_4 , the SOC gives rise to a strong momentum dependence of the FS in direction parallel to the surface normal [Haverkort et al., 2008]. For $\text{Sr}_3\text{Ru}_2\text{O}_7$, recently, the calculations based on the tight-binding model shows that the enclosed electron-like γ on the FS without SOC is broken into an electron-like γ_1 and an hole-like γ_2 pocket (seen in Fig.4.3(b)) after the SOC is included. More importantly, SOC plays a crucial role for the occurrence of the nematic phase [Puetter et al., 2009; Fischer and Sigrist, 2009].

Here, in order to further illustrate the effects of SOC on the band structure in $\text{Sr}_3\text{Ru}_2\text{O}_7$ [Shaked et al., 2000], we have performed local-density approximation (LDA) band-structure calculations with/without SOC, using the full-potential linearized augmented plan-wave density function theory code WIEN2K [Blaha et al., 2008]. Fig.4.17 shows the band dispersion of $\text{Sr}_3\text{Ru}_2\text{O}_7$ calculated with and without SOC. It is clear that SOC results in increased splitting between the bands near E_F . There are several regions in the k-space showing some interesting modifications, such as around M point $(0.5, 0, 0)2\pi/a$ and X point $(0.5, 0.5, 0)2\pi/a$, marked in Fig.4.17(c). Around M point, a band which is above E_F for no SOC situation is lowered to below E_F after the SOC is included, and this band is belong to the quasi 1-D orbital ($d_{xy/yz}$). Around the X point, the position where has a SOC induced hole-like γ_2 pocket, shows a quite different band dispersion for with and without SOC: without SOC, there is only one band coming up to cross E_F and this band forms a small hole-like pocket on the FS; the other band going down to E_F is very close but still above the E_F ; with SOC, these two bands are both shifted in energy and become to both cross the Fermi level, quantitatively, the upper band is shifted down to 6 meV below E_F and the lower band is lifted up to 8.5 meV above E_F , as shown in an

enlarged view in Fig.4.17(d). Therefore, the upper band would produce a small electron-like pocket on the FS, which is the new feature of FS derived from the SOC. The hole-like pocket, which possibly is what we called γ_2 and is corresponding to the magnetic anisotropy, is enlarged by lifting the lower band with SOC and becomes easier to be observed in experiments for the bigger size. Because only small portions of these two bands cross the Fermi level, one can argue that the two corresponding FS pockets could be quite sensitive to the temperature or due to impurities.

The single-layered ruthenates Sr_2RuO_4 has a similar electronic structure [Hossain et al., 2008], but much less number of bands, comparing to the double-layered ruthenates $\text{Sr}_3\text{Ru}_2\text{O}_7$. In order to compare the effect of SOC on the band structures of these two materials, we have performed the LDA+SOC calculation for the Sr_2RuO_4 as well. A comparison for the band dispersions in the bulk and surface calculation is shown in Fig.4.18. Firstly, we obtain the same effect of SOC from the surface calculation of Sr_2RuO_4 with the result from a bulk calculation reported by our group before [Haverkort et al., 2008]. Also similar to the $\text{Sr}_3\text{Ru}_2\text{O}_7$, SOC in Sr_2RuO_4 splits the degenerated bands at Γ point and those between M and X point, and only mildly changes the bands near the E_F . The surface LDA+SOC calculation in Fig.4.18(d) shows the same SOC effect as that in the bulk (Fig.4.18(b)), and it indicates that surface does not affect the band structure unless a specific distortion of the crystal structure is considered. For surface calculation, we use slab approximation consisting in three RuO_2 layers and six SrO_2 layers. Therefore, the number of bands of Ru crossing E_F is three times that of the bulk.

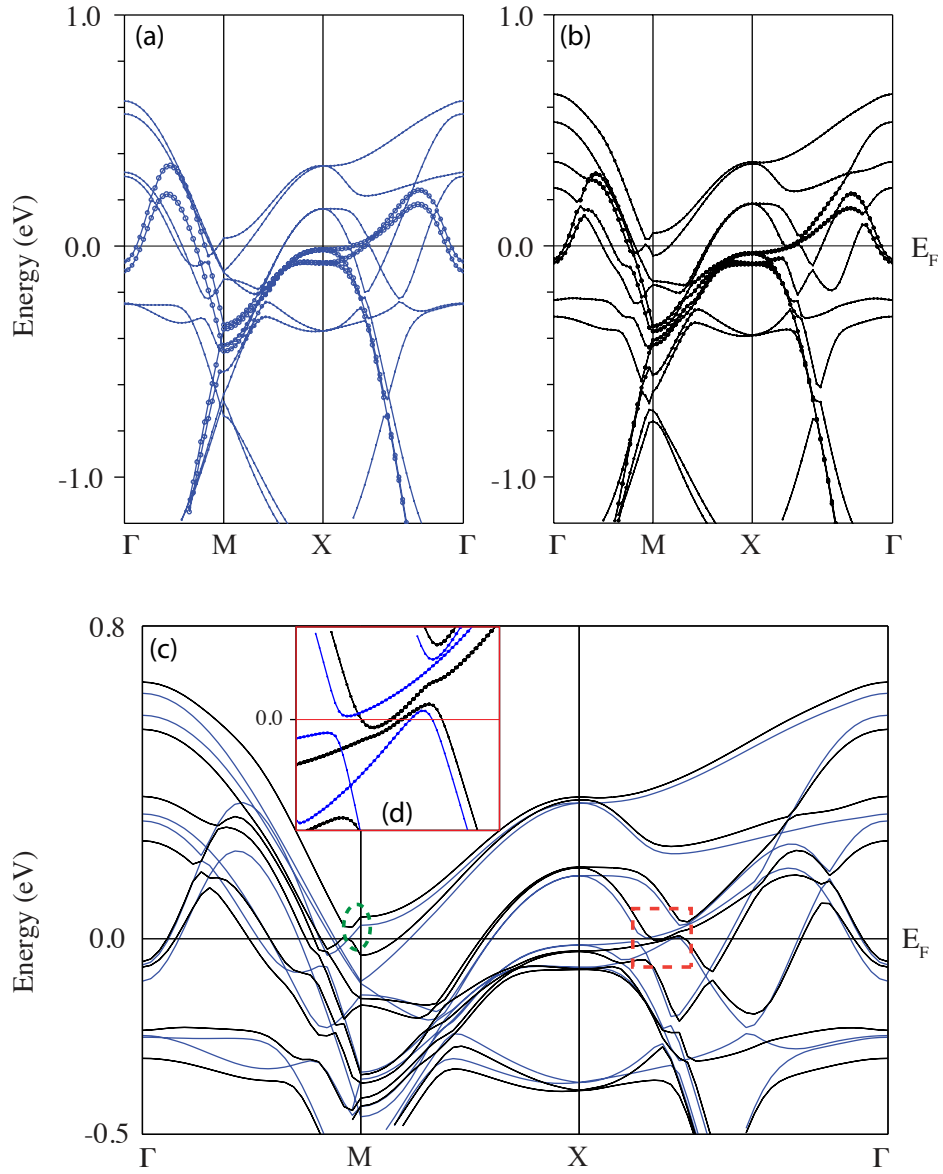


Figure 4.17: (a) LDA and (b) LDA+SOC band dispersion of $\text{Sr}_3\text{Ru}_2\text{O}_7$. d_{xy} bands are highlighted by open circles. (c) The overlap of LDA (blue lines) and LDA+SOC (dark lines) band dispersion. (d) Enlarged view of the marked E_F region in (c).

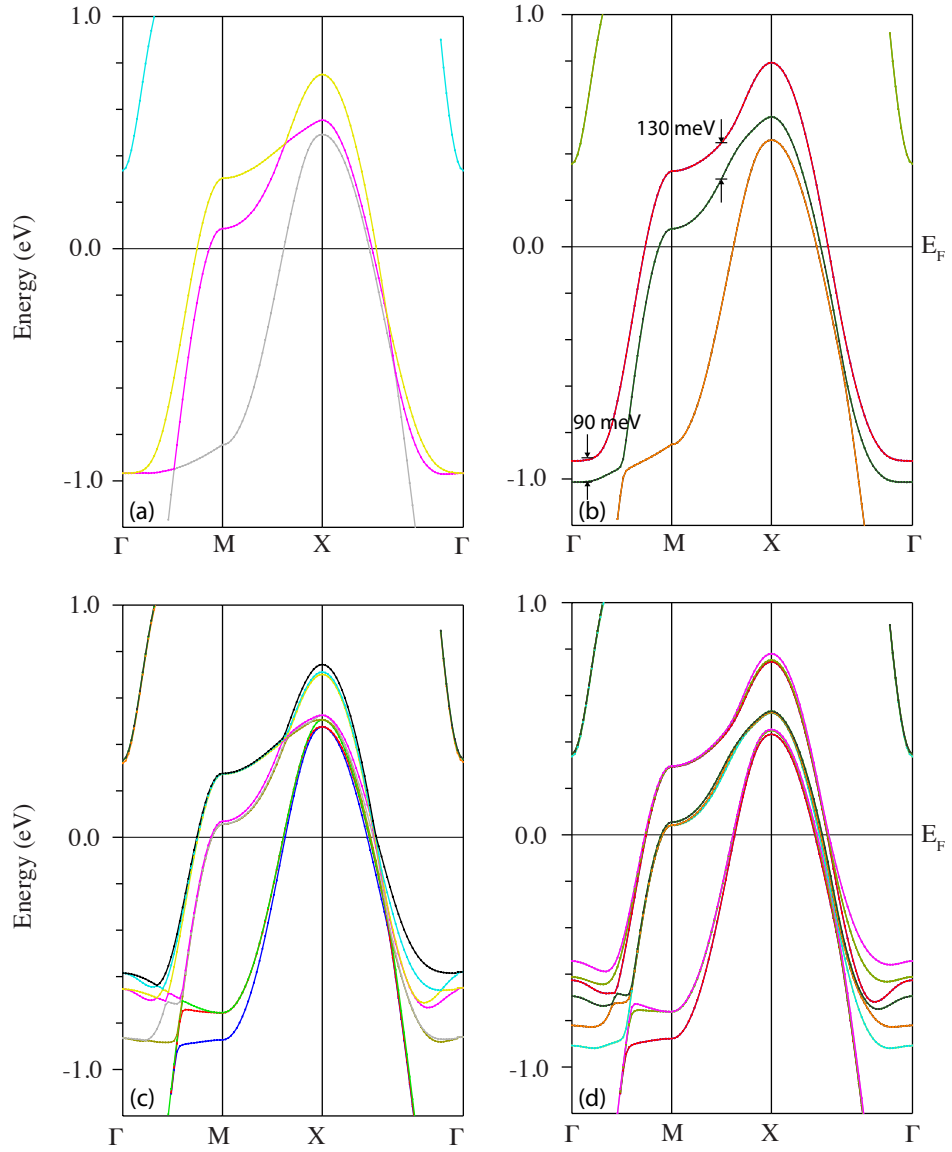


Figure 4.18: LDA: bulk (a) and surface (c), and LDA+SOC: bulk (b) and surface (d), band dispersion of Sr_2RuO_4 .

4.3.6 General discussion

In this section, we will briefly summarize the ARPES experimental results and discuss two key questions: why the nesting vector is inconsistent with the superlattice peak determined from scattering work and how the γ sheet is changed on the FS by Mn doping. As we have shown before, the 1D-featured FS in 10% Mn doped sample has a nesting vector $q_{\alpha\beta}=(0.33, 0.33, 0)$, which is inconsistent with the superlattice peak $q=(0.25, 0.25, 0)$ observed in REXS [Hossain et al., 2009] and the neutron scattering work [Mathieu et al., 2005]. The first thing we need to realize is that ARPES is the surface sensitive technique, but the scattering measurement is sensitive to the bulk properties. The difference between surface and bulk may induce the inconsistency of the nesting vectors. Alternatively, a fact we have to emphasize is that the superlattice peak can only be observed below the MIT temperature T_c . This temperature-determined characteristic of the superlattice peak is a very important point for us to understand why it is inconsistent with the FS-determined nesting vector, since the latter is independent of temperature and only determined by Mn doping level. On the other hand, the nesting vector usually opens a gap on the bands at E_F to lower the electronic energy of the system. The opening of a quasiparticle gap with Mn doping, as shown in section 4.3.4, can thus be understood as a result of the nesting vector. A charge density wave (CDW) corresponding to nesting vector $q_{\alpha\beta}=(0.33, 0.33, 0)$ is from charge/orbital ordering which has a modulation period of 3 lattice constants in real space [Johannes and Mazin, 2008]. The orbital ordering formation has been strongly proposed to be found in the doped layered ruthenates since the discovery of an orbital ordering transition in $\text{La}_4\text{Ru}_2\text{O}_{10}$ [Khalifah et al., 2002]. However, the mechanism of generating such charge ordering by Mn impurities is still unclear and requires us to conduct further studies based on the schematic of Mn induced charge ordering in other systems [Chen et al., 2009; Saniz et al., 2008; S.Mori et al., 1998] or similar to the physical model proposed to explain the REXS superlattice peak (by considering the correlations between Mn impurities) [Hossain et al., 2009]. If we claim that the nesting vector is a result of the charge stripe

4.4. Conclusion

ordering, the superlattice peak $q=(0.25, 0.25, 0)$ is then derived from the combination of antiferromagnetism and charge/orbital orderings, namely a zigzag spin ordering. Because $q=(0.25, 0.25, 0)$ only appears under the T_C of MIT, this fact also indicates that the temperature induced MIT at a fixed Mn doping level is due to a transition from ferromagnetism to antiferromagnetism. Therefore, a possible answer for the first question is that the difference between the charge and spin ordering products the inconsistency between the nesting vector and superlattice peak. A similar discovery of 1D FS and different nesting vectors due to the charge- and spin-ordered state has been reported in $\text{La}_{1.2}\text{Sr}_{1.8}\text{Mn}_2\text{O}_7$ [Chuang et al., 2001].

If we accept the assumption that a charge ordering is formed by Mn impurities, we can further understand the behavior of the missing γ on FS by a 1D system model. Because the charge ordering is 1D structure in the real space, the electron hopping probability t_{ij} would become very anisotropic and electrons would mainly propagate along the ordering direction [Tsuchiizu et al., 2007]. Therefore, the d_{xy} band loses its 2D feature and can only present 1D feature as the same as the $d_{xz/yz}$ bands do. In the 10% Mn doped $\text{Sr}_3\text{Ru}_2\text{O}_7$, the charge ordering makes the α , β and γ sheets become 1D now, and the lifted d_{xy} band by Mn doping lets itself get closer to the β and γ sheets and even be degenerated with each other on the FS. Therefore, we cannot identify the γ sheet on FS any more for its undistinguishable with β sheet and the FS becomes a simple pattern with straight lines.

4.4 Conclusion

The doping and temperature dependence of FS in $\text{Sr}_3(\text{Ru}_{1-x}\text{Mn}_x)_2\text{O}_7$ are investigated through APRES measurements. The 1D FS with a nesting vector $q_{\alpha\beta}=(0.33, 0.33, 0)2\pi/a$ has been observed at 10% Mn doping sample and it indicates that a charge ordering has been formed in the system by Mn doping. The missing γ sheet in the 1D FS has been discussed as a result of the lifted d_{xy} band in the 1D charge ordering system. We demonstrated that a quasiparticle-energy gap opens during the Mn doping induced MIT. And the shift of the Fermi edge with doping level and temperature has been

4.4. Conclusion

measurement. The LDA+SOC calculations on $\text{Sr}_3\text{Ru}_2\text{O}_7$ show that the new features, such as electron-like and hole-like pocket, can be induced by the SOC effect in $\text{Sr}_3\text{Ru}_2\text{O}_7$. The surface and bulk LDA+SOC calculations for the band dispersions of Sr_2RuO_4 show no change of the SOC effect in the surface, in comparison with the bulk.

Chapter 5

Summary

Impurities in complex oxides and in particular transition-metal oxides can introduce profound modifications of the macroscopic physical properties by changing the carrier densities of the host material. More recently, exotic new ways have been discovered to exploit impurity states, in concert with the symmetry and correlated nature of the host materials electronic states, in giving rise to innovative electronic properties. In this thesis, we performed the soft and hard XPS and ARPES to investigate the evolution of electronic behaviors during the metal to insulator transition in $\text{Sr}_3(\text{Ru}_{1-x}\text{Mn}_x)_2\text{O}_7$ with Mn doping. The well screened and unscreened peaks in the PES spectra have been observed in the undoped sample $\text{Sr}_3\text{Ru}_2\text{O}_7$, similar to the two-peak structure in the PES spectra of other ruthenate oxides. The screened peak, located at about 1.0 eV lower binding energy than that of the rather broad unscreened peak, is suppressed as the system becomes more insulating with higher Mn concentration, indicating that the screening channel is very sensitive to the impurities and is proportional to metallicity of the system. The charge-transfer mechanism as described in $3d$ cuprates is not adequate to explain the appearance of these screened peaks, because the electron correlation effect in $4d$ orbitals is weak and then ruthenate oxides is belong to the Mott-Hubbard model, where the oxygens cannot involve the core-hole screening process. However, a screening by conduction electrons from the coherent band is possible to elucidate the origin of the screened peak, and we are using a multi-Ru site cluster model to verify this propose now.

The investigation of metal-insulator transition through the changes of FS measured by ARPES is usually rather challenging because of the corresponding decrease in spectral intensity and broadening of the ARPES features in the insulator. However, our ARPES measurement of Mn doped

sample showed that high-quality data can be obtained even at 10%Mn doping level, and an important change in the nesting condition is observed with increasing Mn concentration. For example, the FS topology, mainly including two 1-D α and β sheets from $d_{xz/yz}$ bands and one 2-D γ sheet from d_{xy} band in the undoped sample, becomes a pattern with only 1-D sheets at 10% Mn doping level. This dramatic change of the FS topology suggests that the Mn impurities either introduce some charge/orbital ordering into the system, or have reconstructed the electrons distribution on the valence bands of Ru. The band dispersions checked by MDCs show that the d_{xy} band possibly has been lifted up to a lower binding energy and becomes degenerated with its neighboring $d_{xy/yz}$ bands, resulting the disappearance of the 2-D γ sheet on the FS. However, we cannot observe any evidence similar to that explaining the missing 2-D γ sheet in another ruthenates $\text{Ca}_{1.8}\text{Sr}_{0.2}\text{RuO}_4$, where the energy level of the d_{xy} bands is lowered to below E_F due to a crystal field from the Ca induced rotation of RuO_6 octahedra. On the other hand, the opening of an energy gap is observed as large as 50 meV accompanied by the MIT.

The spin-orbital coupling effect on the band structure in $\text{Sr}_3\text{Ru}_2\text{O}_7$ has been studied by LDA+SOC calculation. It shows that the FS modifications are subtle but equally dramatic in the detail: spin-orbital coupling induced a new electron-like pocket and enlarged a small hole-like pocket around X point, and a new electron pocket around M point. These findings have profound implications for the understanding the nematic phase in $\text{Sr}_3\text{Ru}_2\text{O}_7$.

Bibliography

- For a review on correlated electron systems. *Science*, 288:389–564, 2000.
- P. W. Anderson. Localized magnetic states in metals. *Phys. Rev.*, 124:41, 1961.
- V. I. Anisimov, I.A. Nekrasov, D.E. Kondakov, T.M. Rice, and M. Sigrist. Orbital-selective mott-insulator transition in $\text{Ca}_{2-x}\text{Sr}_x\text{RuO}_4$. *Eur. Phys. J. B*, 25:191, 2002.
- F. Baumberger, N. J. C. Ingle, N. Kikugawa, M. A. Hossain, W. Meevasana, R. S. Perry, K. M. Shen, D. H. Lu, A. Damascelli, A. Rost, A. P. Mackenzie, Z. Hussain, and Z.-X. Shen. Nested fermi surface and electronic instability in $\text{Ca}_3\text{Ru}_2\text{O}_7$. *Phys. Rev. Lett.*, 96:107601, 2006.
- C. Bergemann, A. P. Mackenzie, S. R. Julian, D. Forsythe, and E. Ohmichi. Quasi-two-dimensional fermi liquid properties of the unconventional superconductor Sr_2RuO_4 . *Advances in Physics*, 52:639, 2003.
- C. Bergemann, S. R. Julian, A. P. Mackenzie, S. NishiZaki, and Y. Maeno. Detailed topography of the fermi surface of Sr_2RuO_4 . *Phys. Rev. Lett.*, 84:2662, 2000.
- Peter Blaha, Karlheinz Schwarz, Georg K. H. Madsen, Dieter Kvasnicka, and Joachim Luitz. *An Augmented Plane Wave + Local Orbitals Program for Calculation Crystal Properties*. edited by K. Schwarz Technical Unisersity of Wien, A-1060 Wien/Austria, wien2k 08.3 edition, 2008.
- A.E. Bocquet, T. Mizokawa, T. Saitoh, H. Namatame, and A. Fujimori. Electronic structure of 3d-transition-metal compounds by analysis of the 2p core-level photoemission spectra. *Phys. Rev. B*, 46:3771, 1992.

Bibliography

- R. Borzi, S. A. Grigera, J. Farrell, R. S. Perry, S. J. S. Lister, S. L. Lee, D. A. Tennant, Y. Maeno, and A. P. Machenzie. Formation of a nematic fluid at high fields in $\text{Sr}_3\text{Ru}_2\text{O}_7$. *Science*, 315:214, 2007.
- A. Callaghan, C. W. Moeller, and R. Ward. Magnetic interactions in ternary ruthenium oxides. *Inorg. Chem.*, 5:1572, 1966.
- J. M. Chen, J. M. Lee, C. K. Chen, T. L. Chou, K. T. Lu, S. C. Haw, K. S. Liang, C. T. Chen, H. T. Jeng, S. W. Huang, T. J. Yang, C. C. Shen, R. S. Liu, J. Y. Lin, and Z. Hu. Bonding anisotropy in multiferroic TbMnO_3 probed by polarization dependent x-ray absorption spectroscopy. *Appl. Phys. Lett.*, 94:044105, 2009.
- Y.-D. Chuang, A. D. Gromko, D. S. Dessau, T. Kimura, and Y. Tokura. Fermi surface nesting and nanoscale fluctuating charge/orbital ordering in colossal magnetoresistive oxides. *Science*, 292:1509, 2001.
- M. K. Crawford, R. L. Harlow, W. Marshall, Z. Li, G. Cao, R. L. Lindstrom, Q. Huang, and J. W. Lynn. Structure and magnetism of single crystal $\text{Sr}_4\text{Ru}_3\text{O}_{10}$: a ferromagnetic triple-layer ruthenate. *Phys. Rev. B*, 65:214412, 2002.
- A. Damascelli. Probing the electronic structure of complex systems by ARPES. *Physica Scripta. Vol.*, T109:61, 2004.
- A. Damascelli, D. H. Lu, K. M. Shen, N. P. Armitage, F. Ronning, D. L. Feng, C. Kim, T. Kimura, Y. Tokura, Z. Q. Mao, Y. Maeno, and Z.-X. Shen. Fermi surface, surface states, and surface reconstruction in Sr_2RuO_4 . *Phys. Rev. Lett.*, 85:5194, 2000.
- A. Damascelli, D. H. Lu, K. M. Shen, and Z.-X. Shen. Damascelli *et al* reply. *Phys. Rev. Lett.*, 87:239702, 2001.
- A. Damascelli, Z. Hussain, and Z. X. Shen. Angle-resolved photoemission studies of the cuprate superconductors. *Rev. Mod. Phys.*, 75:473, 2003.

- V. Durairaj, S. Chikara, X. N. Lin, A. Douglass, G. Cao, P. Schlottmann, E. S. Choi, and R. P. Guertin. Highly anisotropic magnetism in Cr-doped perovskite ruthenates. *Phys. Rev. B*, 73:214414, 2006.
- H. Eskes and G. A. Sawatzky. Tendency towards local spin compensation of holes in the High- T_c copper compounds. *Phys. Rev. Lett.*, 61:1415, 1988.
- Eric Fawcett. Spin-density-wave antiferromagnetism in chromium. *Rev. Mod. Phys.*, 60:209, 1988.
- M. H. Fischer and M. Sigrist. Effect of a staggered spin-orbit coupling on the occurrence of a nematic phase in $\text{Sr}_3\text{Ru}_2\text{O}_7$. *arXiv*, 0909:5392v1, 2009.
- A. Fujimori, E. Takayama-Muromachi, Y. Uchida, and B. Okai. Spectroscopic evidence for strongly correlated electronic states in La-Sr-Cu and Y-Ba-Cu oxides. *Phys. Rev. B*, 35:8814, 1987.
- S. Grigera, R. Perry, A. Schofield, M. Chiao, S. R. Julian, G. G. Lonzarich, S. I. Ikeda, Y. Maeno, A. J. Millis, and A. P. Mechenzie. Magnetic field-tuned quantum criticality in the metallic ruthenate $\text{Sr}_3\text{Ru}_2\text{O}_7$. *Science*, 294:329, 2001.
- S. A. Grigera, P. Gegenwart, R. A. Borzi, F. Weichert, A. J. Schofield, R. S. Perry, T. Tayama, T. Sakakibara, Y. Maeno, A. G. Green, and A. P. Mackenzie. Disorder-sensitive phase formation linked to metamagnetic quantum criticality. *Science*, 306:5699, 2004a.
- S. A. Grigera, R. S. Perry, A. J. Schofield, M. Chiao, S. R. Julian, G. G. Lonzarich, S. I. Ikeda, Y. Maeno, A. J. Millis, and A. P. Mackenzie. Magnetic field-tuned quantum criticality in the metallic ruthenates $\text{Sr}_3\text{Ru}_2\text{O}_7$. *Science*, 306:1154, 2004b.
- M. W. Haverkort, I. S. Ifimov, L. H. Tjeng, G. A. Sawatzky, and A. Damascelli. Strong spin-orbit coupling effects on the fermi surface of Sr_2RuO_4 and Sr_2RhO_4 . *Phys. Rev. Lett.*, 101:026406, 2008.

- K. Held, G. Keller, V. Eyert, D. Vollhart, and V. I. Anisimov. Mott-hubbard metal-insulator transition in paramagnetic V_2O_3 : An LDA+DMFT study. *Phys. Rev. Lett.*, 86:5345, 2001.
- H. Hertz. Ü einen Einfluss des ultravioletten Lichtes auf die elektrische Entladung (on the influence of ultraviolet light on the electric discharge. *Ann. Physik*, 31:983, 1887.
- K. Horiba, M. Taguchi, A. Chainani, Y. Takata, E. Ikenaga, D. Miwa, Y. Nishino, K. Tamasaku, M. Awaji, A. Takeuchi, M. Yabashi, H. Namatame, M. Taniguchi, H. Kumigashira, M. Oshima, M. Lippmaa, M. Kawasaki, H. Koinuma, K. Kobayashi, T. Ishikawa, and S. Shin. Nature of the well screened state in hard x-ray Mn $2p$ core-level photoemission measurements of $La_{1-x}Sr_xMnO_3$ films. *Phys. Rev. Lett.*, 93:236401, 2004.
- M. A. Hossain, Z. Hu, M. W. Haverkort, T. Burnus, C. F. Chang, S. Klein, J. D. Denlinger, H. J. Lin, C. T. Chen, R. Mathieu, Y. Kaneko, Y. Tokura, S. Satow, Y. Yoshida, H. Takagi, A. Tanaka, I. S. Elfimov, G. A. Sawatzky, L. H. Tjeng, and A. Damascelli. Crystal-field level inversion in lightly Mn-doped $Sr_3Ru_2O_7$. *Phys. Rev. Lett.*, 101:016404, 2008.
- M. A. Hossain, B. Bohnenbuck, Y.-D. Chuang, A.G. Cruz Gonzalez, I. Zegkinoglou, M.W. Haverkort, J. Geck, D.G. Hawthorn, H.-H. Wu, C. Schüler-Langeheine, R. Mathieu, Y. Tokura, S. Satow, H. Takagi, Y. Yoshida, J.D. Denlinger, I.S. Elmov, Z. Hussain, B. Keimer, G.A. Sawatzky, and A. Damascelli. Magnetic superstructure and metal-insulator transition in Mn-substituted $Sr_3Ru_2O_7$. *arXiv*, 0906:0035, 2009.
- Q. Huang, J. W. Lynn, R. W. Erwin, J. Jarupatrakorn, and R. J. Cava. Oxygen displacements and search for magnetic order in $Sr_3Ru_2O_7$. *Phys. Rev. B*, 58:8515, 1998.
- S. Hüfner and G.K. Wertheim. Multielectron effects in the XPS spectra of nickel. *Phys. Lett. A*, 51 A:299, 1975.

- Stefan Hüfner. *Photoelectron Spectroscopy*, volume 82 of *Solid-State Sciences*. Springer-Verlag, Berlin, 1995.
- S. I. Ikeda, Y. Maeno, S. Nakatsuji, M. Kosaka, and Y. Uwatoko. Ground state in $\text{Sr}_3\text{Ru}_2\text{O}_7$: Fermi liquid close to a ferromagnetic instability. *Phys. Rev. B*, 62:R6089, 2000.
- M. Imada, A. Fujimori, and Y. Tokura. Metal-insulator transitions. *Rev. Mod. Phys.*, 70:1039, 1998.
- N. J. C. Ingle, K. M. Shen, F. Baumberger, W. Meevasana, D. H. Lu, A. Damascelli, S. Nakatsuji, Z. Q. Mao, Y. Maeno, T. Kimura, Y. Tokura, and Z.-X. Shen. Quantitative analysis of Sr_2RuO_4 angle-resolved photoemission spectra: Many-body interactions in a model fermi liquid. *Phys. Rev. B*, 72:205114, 2005.
- M. D. Johannes and I. I. Mazin. Fermi surface nesting and the origin of charge density waves in metals. *Phys. Rev. B*, 77:165135, 2008.
- P. Khalifah, R. Osborn, Q. Huang, H. W. Zandbergen, R. Jin, Y. Liu, D. Mandrus, and R. J. Cava. Orbital ordering transition in $\text{La}_4\text{Ru}_2\text{O}_{10}$. *Science*, 297:2237, 2002.
- B. J. Kim, Jaejun Yu, H. Koh, I. Nagai, S. I. Ikeda, S.-J. Oh, and C. Kim. Missing xy -band fermi surface in $4d$ transition-metal oxide Sr_2RhO_4 : Effect of the octahedra rotation on the electronic structure. *Phys. Rev. Lett.*, 97:106401, 2006.
- Hyeong-Do Kim, Han-Jin Noh, K. H. Kim, and S.-J. Oh. Core-level x-ray photoemission satellites in Ruthenates: A new mechanism revealing the mott transition. *Phys. Rev. Lett.*, 93:126404, 2004.
- Y Klein, S Hébert, and A Maignan. Insensitivity of the band structure of substituted SrRuO_3 as probed by seebeck coefficient measurements. *Phys. Rev. B*, 73:052412, 2006.
- T. Koopmans. Ordering of wave functions and eigenenergies to the individual electrons of an atom. *Physica*, 1:104, 1933.

- N. D. Lang and W. Kohn. Theory of metal surface: Work function. *Phys. Rev. B*, 3:1215, 1971.
- S. Larsson. Theory of satellite excitations in inner shell x-ray photoelectron spectra of nickel and copper compounds. *Chem. Phys. Lett.*, 32:401, 1975.
- Guo-Qiang Liu, V. N. Antonov, O. Jepsen, and O. K. Andersen. Coulomb-enhanced spin-orbit splitting: The missing piece in the Sr_2RhO_4 puzzle. *Phys. Rev. Lett.*, 101:026408, 2008.
- A. P. Mackenzie, Shin ichi Ikeda, Y. Meano, T. Fujita, S. R. Julian, and G. G. Lonzarich. The fermi surface topography of Sr_2RuO_4 . *J. Phys. Soc. Jpn.*, 67:385, 1998.
- A. P. Mackenzie and Y. Maeno. The superconductivity of Sr_2RuO_4 and the physics of spin-triplet pairing. *Rev. Mod. Phys.*, 75:657, 2003.
- R. Mathieu, A. Asamitsu, Y Kaneko, J. P. He, X. Z. Yu, R. Kumai, Y. Onose, N. Takeshita, T. Arima, H. Takagi, and Y. Tokura. Impurity-induced transition to a mott insulator in $\text{Sr}_3\text{Ru}_2\text{O}_7$. *Phys. Rev. B*, 72:092404, 2005.
- T. Mizokawa, L. H. Tjeng, G. A Sawatzky, G. Ghiringhelli, O. Tjernberg, N. B. Brookes, H. Fukazawa, S. Nakatsuji, and Y. Maeno. Spin-orbit coupling in the mott insulator Ca_2RuO_4 . *Phys. Rev. Lett.*, 87:077202, 2001.
- S.-K. Mo, J. D. Denlinger, H.-D. Kim, J.-H. Park, J. W. Allen, A. Sekiyama, A. Yamasaki, K. Kadono, S. Suga, Y. Saitoh, T. Muro, P. Metcalf, G. Keller, K. Held, V. Eyert, V. I. Anisimov, and D. Vollhardt. Prominent quasiparticle peak in the photoemission spectrum of the metallic phase of V_2O_3 . *Phys. Rev. Lett.*, 90:186403, 2003.
- M. Neupane, R. Richard, Z.-H. Pan, Y.-M. Xu, R. Jin, D. Mandrus, X. Dai, Z. Fang, Z. Wang, and H. Ding. Observation of a novel orbital selective mott transition in $\text{Ca}_{1.8}\text{Sr}_{0.2}\text{RuO}_4$. *Phys. Rev. Lett.*, 103:097001, 2009.

- Han-Jin Noh. *Electron Spectroscopy Study of Ruthenium Oxides and Manganese Oxides*. PhD dissertation, Seoul National University, August 2003.
- T. Oguchi. Spin-orbit effects on the Ru-*d* orbital hybridiation and fermi surface in $\text{Ca}_{2-x}\text{Sr}_x\text{RuO}_4$. *J. Phys. Soc. Jpn.*, 78:044702, 2009.
- Kozo Okada. Multisite effects on the core-level photoemission in Sr_2RuO_4 . *Surf. Rev. Lett.*, 9:1023, 2002.
- Kozo Okada. Electronic structure of $\text{Nd}_{2-x}\text{Ce}_x\text{CuO}_4$ and $\text{La}_{2-x}\text{Sr}_x\text{CuO}_4$ deduced from Cu 2*p* photoemission and photoabsorption. *J. Phys. Soc. Jpn.*, 78:034725, 2009.
- G. Panaccione, G. Cautero, M. Cautero, A. Fondacaro, M. Grioni, P. Lacovig, G. Monaco, F. Offi, G. Paolicelli, M. Sacchi, N. Stojić, G. Stefani, R. Tommasin, and P. Torelli. High-energy photoemission in silver: resolving *d* and *sp* contributions in valence band spectra. *J. Phys.: Condens. Matter*, 17:2671, 2005.
- G. Panaccione, M. Altarelli, A. Fondacaro, A. Georges, S. Huotari, P. Lacovig, A. Lichtenstein, P. Metcalf, G. Monaco, F. Offi, L. Paolasini, A. Poteryaev, O. Tjernberg, and M. Sacchi. Coherent peaks and minimal probing depth in photoemission spectroscopy of Mott-Hubbard systems. *Phys. Rev. Lett.*, 97:116401, 2006.
- G. Panaccione, I. Vobornik, J. Fujii, D. Krizmancic, E. Annese, L. Giovanelli, F. Maccherozzi, F. Salvador, A. De Luisa, D. Benedetti, A. Gruden, P. Bertoch, F. Polack, D. Cocco, G. Sostero, B. Diviaco, M. Hochstrasser, U. Maier, D. Pescia, C. H. Back, T. Greber, J. Osterwalder, M. Galaktionov, M. Sancrotti, and G. Rossi. Advanced photoelectric effect experiment beamline at elettra: A surface science laboratory coupled with synchrotron radiation. *Rev. Sci. Instrum.*, 80:043105, 2009.
- J. Park, S. Ryu, M.-S. Han, and S.-J. Oh. Charge-transfer satellites in the 2*p* core-level photoelectron spectra of heavy-transition-metal dihalides. *Phys. Rev. B*, 37:10867, 1988.

- Hermen Folken Pen. *High energy spectroscopy on vanadium oxides: electronic structure and phase transitions*. PhD dissertation, University of Groningen, September 1997.
- Li Pi, A Maignan, R Retoux, and B Raveau. Substitution at the Ru site in the itinerant ferromagnet SrRuO_3 . *J. Phys.: Condens. Matter*, 14:7391, 2002.
- A. I. Poteryaev, J. M. Tomczak, S. Biermann, A. Georges, A. I. Lichtenstein, A. N. Rubtsov, T. Saha-Dasgupta, and O. K. Andersen. Enhanced crystal-field splitting and orbital-selective coherence induced by strong correlations in V_2O_3 . *Phys. Rev. B*, 76:085127, 2007.
- C. M. Puetter, J. G. Rau, and H. Y. Kee. Microscopic route to nematicity in $\text{Sr}_3\text{Ru}_2\text{O}_7$. *arXiv*, 0909:4545v1, 2009.
- F. Rodolakis, B. Mansart, E. Papalazarou, S. Gorovikov, P. Vilmercati, L. Petaccia, A. Goldoni, J. P. Rueff, S. Lupi, P. Metcalf, and M. Marsi. Quasiparticles at the mott transition in V_2O_3 : Wave vector dependence and surface attenuation. *Phys. Rev. Lett.*, 102:066805, 2009.
- M. Sacchi, F. Offi, P. Torelli, A. Fondacaro, C. Spezzani, M. Cautero, G. Cautero, S. Huotari, M. Grioni, R. Delaunay, M. Fabrizioli, G. Vankó, G. Monaco, G. Paolicelli, G. Stefani, and G. Panaccione. Quantifying the effective attenuation length in high-energy photoemission experiments. *Phys. Rev. B*, 71:155117, 2005.
- R. Saniz, M. R. Norman, and A.J. Freeman. Orbital mixing and nesting in the bilayer manganites $\text{La}_{2-2x}\text{Sr}_{1+2x}\text{Mn}_2\text{O}_7$. *Phys. Rev. Lett.*, 101:236402, 2008.
- A. Sekiyama, H. Fujiwara, S. Imada, S. Suga, H. Eisaki, S. I. Uchida, K. Takegahara, H. Harima, Y. Saitoh, I. A. Nekrasov, G. Kelle, D. E. Kondakov, A. V. Kozhevnikov, Th. Pruschke, K. Held, D. Vollhardt, and V. I. Anisimov. Mutual experimental and theoretical validation of bulk photoemission spectra of $\text{Sr}_{1-x}\text{Ca}_x\text{VO}_3$. *Phys. Rev. Lett.*, 93:156402, 2004a.

- A. Sekiyama, S. Kasai, M. Tsunekawa, Y. Ishida, M. Sing, A. Irizawa, A. Yamasaki, S. Imada, T. Muro, Y. Saitoh, Y. Onuki, T. Kimura, Y. Tokura, and S. Suga. Technique for bulk fermiology by photoemission applied to layered ruthenates. *Phys. Rev. B*, 70:060506(R), 2004b.
- H. Shaked, J. D. Jorgensen, O. Chmaissem, S. Ikeda, and Y. Maeno. Neutron diffraction study of the structural distortions in $\text{Sr}_3\text{Ru}_2\text{O}_7$. *J. Phys. Soc. Jpn.*, 154:361, 2000.
- K. M. Shen, A. Damascelli, D. H. Lu, N. P. Armitage, F. Ronning, D. L. Feng, C. Kim, D. J. Singh, I. I. Mazin, S. Nakatsuji, Z. Q. Mao, Y. Maeno, T. Kimura, Y. Tokura, and Z.-X. Shen. Surface electronic structure of Sr_2RuO_4 . *Phys. Rev. B*, 64:180502(R), 2001.
- Z.X. Shen, J.W. Allen, J.J. Yeh, J.-S. Kang, W. Ellis, W. Spicer, I. Lindau, M.B. Maple, Y.D. Dlichouch, J.Z. Sun M.S. Torikachvili, and T.H. Geballe. Anderson hamiltonian description of the experimental electronic structure and magnetic interactions of copper oxide superconductors. *Phys. Rev. B*, 36:8414, 1987.
- D. J. Singh. Relationship of Sr_2RuO_4 to the superconducting layered cuprates. *Phys. Rev. B*, 52:1358, 1995.
- D. J. Singh and I. I. Mazin. Electronic structure and magnetism of $\text{Sr}_3\text{Ru}_2\text{O}_7$. *Phys. Rev. B*, 63:165101, 2001.
- S.Mori, C. H. Chen, and S.-W. Cheong. Pairing of charge-ordered stripes in $(\text{La,Ca})\text{MnO}_3$. *Nature*, 392:473, 1998.
- V. N. Strocov, H. I. Starnberg, P. O. Nilsson, H. E. Brauer, , and L. J. Holleboom. New method for absolute band structure determination by combining photoemission with very-low energy electron diffractions: Application to layered VSe_2 . *Phys. Rev. Lett.*, 79:467, 1997.
- V. N. Strocov, R. Claessen, G. Nicolay, S. Hüfner, A. Kimura, A. Harasawa, S. Shin, A. Kakizaki, P. O. Nilsson, H. I. Starnberg, and P. Blaha. Absolute band mapping by combined angle-dependent very-low-energy electron

diffraction and photoemission: Application to Cu. *Phys. Rev. Lett.*, 81: 4943, 1998.

M. Taguchi, A. Chainani, N. Kamakura, K. Horiba, Y. Takata, M. Yabashi, K. Tamasaku, Y. Nishino, D. Miwa, T. Ishikawa, S. Shin, E. Ikenaga, T. Yokoya, K. Kobayashi, T. Mochiku, K. Hirata, and K. Motoya. Bulk screening in core-level photoemission from Mott-Hubbard and charge-transfer systems. *Phys. Rev. B*, 71:155102, 2005.

M. Takizawa, D. Toyota, H. Wadati, A. Chikamatsu, H. Kumigashira, A. Fujimori, M. Oshima, Z. Fang, M. Lippmaa, M. Kawasaki, and H. Koinuma. Manifestation of correlation effects in the photoemission spectra of $\text{Ca}_{1-x}\text{Sr}_x\text{RuO}_3$. *Phys. Rev. B*, 72:060404, 2005.

A. Tamai, M. P. Allan, J. F. Mercure, W. Meevasana, R. Dunkel, D. H. Lu, R. S. Perry, A. P. Meckenzie, D. J. Singh, Z.-X. Shen, and F. Baumberger. Fermi surface and van hove singularities in the itinerant metamagnet $\text{Sr}_3\text{Ru}_2\text{O}_7$. *Phys. Rev. Lett.*, 101:026407, 2008.

P. Torelli, M. Sacchi, G. Cautero, M. Cautero, B. Krastanov, P. Pittana, P. Lacovig, R. Sergo, R. Tommasini, A. Fondacaro, F. Offi, G. Paolicelli, G. Stefani, M. Grioni, R. Verbeni, G. Monaco, and G. Panaccione. Experimental setup for high energy photoemission using synchrotron radiation. *Rev. Sci. Instrum.*, 76:023909, 2005.

M. Tsuchiizu, Y. Suzumura, and C. Bourbonnais. Interchain-frustration-induced metallic state in quasi-one-dimensional mott insulators. *Phys. Rev. Lett.*, 99:126404, 2007.

G. van der Laan, C. Westra, C. Haas, and G.A. Sawatzky. Satellite structure in photoelectron and Auger spectra of copper dihalides. *Phys. Rev. B*, 23: 4369, 1981.

M.A. Van Veenendaal. Competition between screening channels in core-level x-ray photoemission as a probe of changes in the ground-state properties of transition-metal compounds. *Phys. Rev. B*, 74:085118, 2006.

- M.A. Van Veenendaal and G.A. Sawatzky. Nonlocal screening effects in $2p$ x-ray photoemission spectroscopy core-level line shapes of transition metal compounds. *Phys. Rev. Lett.*, 70:2459, 1993.
- M.A. Van Veenendaal, H. Eskes, and G.A. Sawatzky. Strong nonlocal contributions to Cu $2p$ photoelectron spectroscopy. *Phys. Rev. B*, 47:11462, 1993.
- S.-C. Wang, H.-B. Yang, A. K. P. Sekharan, S. Souma, H. Matsui, T. Sato, T. Takahashi, Chenxi Lu, Jiandi Zhang, R. Jin, D. mandrus, E. W. Plummer, Z. Wang, and H. Ding. Fermi surface topology of $\text{Ca}_{1.5}\text{Sr}_{0.5}\text{RuO}_4$ determined by angle-resolved photoelectron spectroscopy. *Phys. Rev. Lett.*, 93:177007, 2004.
- A. J. Williams, A. Gillies, J. P. Attfield, G. Heymann, H. Huppertz, M. J. Martínez-Lope, and J. A. Alonso. Charge transfer and antiferromagnetic insulator phase in $\text{SrRu}_{1-x}\text{Cr}_x\text{O}_3$ perovskites: Solid solutions between two itinerant electron oxides. *Phys. Rev. B*, 73:104409, 2006.
- J. Zaanen, G.A. Sawatzky, and J.W. Allen. Band gaps and electronic structure of transition-metal compounds. *Phys. Rev. Lett*, 55:418, 1985.
- J. Zaanen, C. Westra, and G.A. Sawatzky. Determination of the electronic structure of transition-metal compounds: $2p$ x-ray photoemission spectroscopy of the nickel dihalides. *Phys. Rev. B*, 33:8060, 1986.
- F.C. Zhang and T.M. Rice. Effective hamiltonian for the superconducting Cu oxides. *Phys. Rev. B*, 37:3759, 1988.